Published in final edited form as:
Cell Rep. 2025 March 25; 44(3): 115328. doi:10.1016/j.celrep.2025.115328.

Real-time visualization reveals *Mycobacterium tuberculosis* ESAT-6 disrupts phagosome-like compartment via fibril-mediated vesiculation

Debraj Koiri[1,5], **Mintu Nandi**[#2], **P.M. Abik Hameem**[#1,5], **Jayesh Bhausaheb Aher**[1,5], **Akhil Kumar**[3], **Assirbad Behura**[1,5], **Geetanjali Meher**[1,5], **Vineet Choudhary**[3], **Sandeep Choubey**[4,5], **Mohammed Saleem**[1,5,6,8,*]

[1]School of Biological Sciences, National Institute of Science Education & Research (NISER), Bhubaneshwar, India.

[2]Department of Chemistry, Indian Institute of Engineering Science and Technology, Shibpur, India.

[3]Department of Biotechnology, All India Institute of Medical Sciences, New Delhi, India.

[4]Institute of Mathematical Sciences (IMSc), Chennai, India.

[5]Homi Bhabha National Institute (HBNI), Mumbai, India.

[6]Center for Interdisciplinary Sciences, National Institute of Science Education & Research (NISER), Bhubaneshwar, India.

[#] These authors contributed equally to this work.

Summary

Mycobacterium tuberculosis (*Mtb*) evades host defense by hijacking and rupturing the phagosome. ESAT-6, a secreted virulence protein of *Mtb*, is known to be critical for phagosome rupture. However, the mechanism of ESAT-6-mediated disruption of the phagosomal membrane remains unknown. Using *in vitro* reconstitution, live-cell imaging, and numerical simulations, we discover that ESAT-6 polymerization forces remodeling and vesiculation of the phagosome-like compartment both *in vitro* and *in vivo*. Shallow insertion of ESAT-6 leads to tubular and bud-like deformations on the membrane facilitated by a reduction in membrane tension. Growing fibrils generate both radial and tangential forces causing local remodeling and shape transition of the membrane into buds. The ESAT-6-bound tensed membrane undergoes local changes in membrane curvature and lipid phase separation that assist the subsequent fission. Overall, the findings

[*]Correspondence: saleem@niser.ac.in .
[8]Lead contact

Author Contributions

Conceptualization, D.K. and M.S.; methodology, D.K., M.N., A.H.P.M., J.B.A., A.K., and A.B.; investigation, D.K., M.N., A.H., J.B.A., A.K., and A.B.; formal analysis, D.K., M.N., G.M., S.C., and M.S.; resources, A.B., M.N., S.C., and V.C.; writing – original draft, D.K. and M.S.; writing – review & editing, S.C. and M.S.; data curation, D.K. and M.S.; funding acquisition, M.S., overall supervision, M.S.

Declaration of Interests

The authors declare no competing interests.

Europe PMC Funders Author Manuscripts

provide mechanistic insights into the long-standing question of phagosome disruption by *Mtb* for its escape.

Abstract

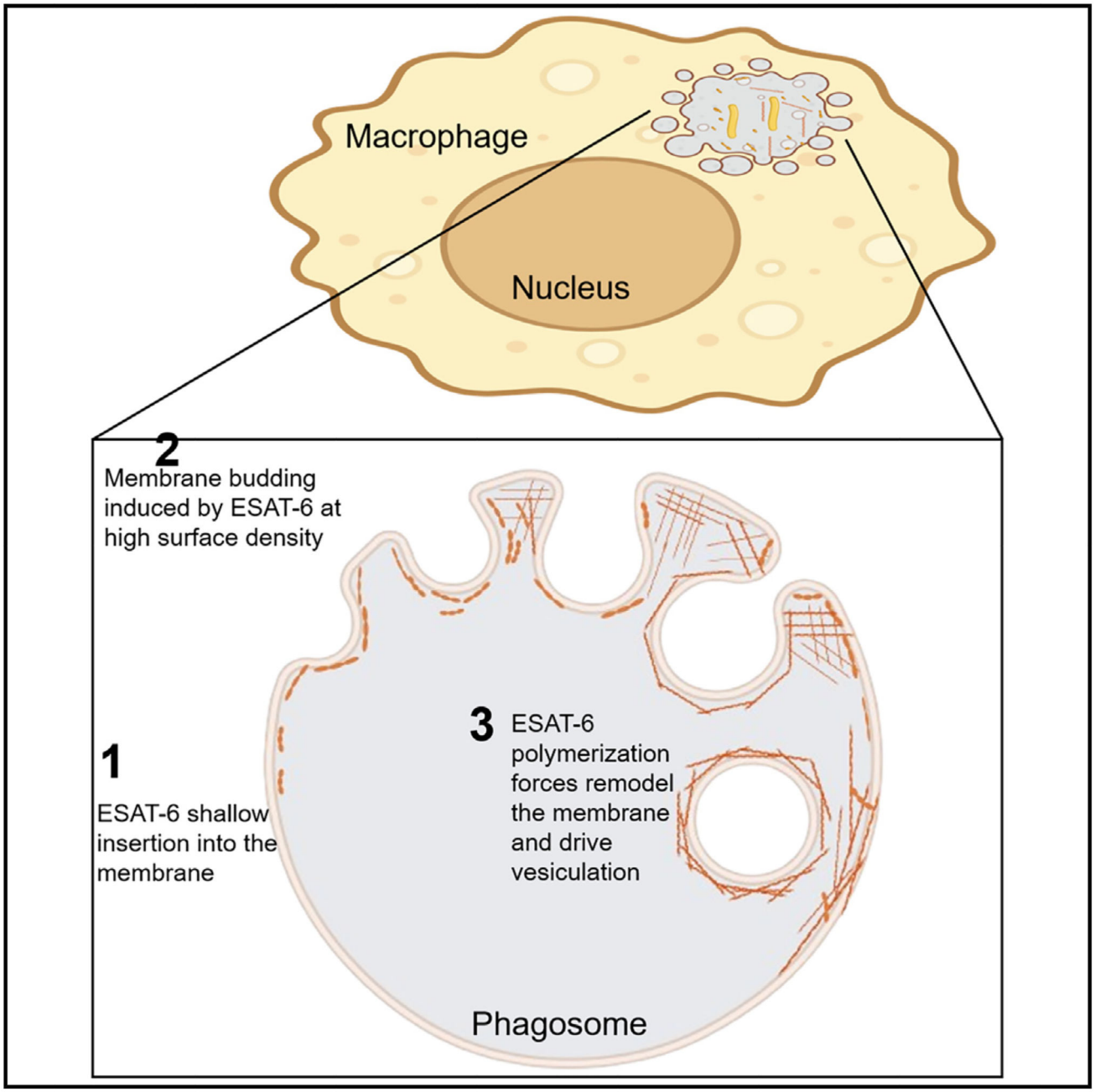

Graphical abstract.

Europe PMC Funders Author Manuscripts

Introduction

Mycobacterium tuberculosis (*Mtb*), the causative agent of tuberculosis, survives inside the host by regulating phagosome maturation and rupture to escape into the cytosol of the host cell.[1] ESAT-6 (6 kDa early secretory antigen target), also called EsxA as per current nomenclature, is a highly immunogenic effector secreted by *Mtb* and has been identified as a critical protein involved in the process of phagosome (also referred to as *Mycobacteria*-containing vacuole) rupture.[2] ESAT-6 is known to be secreted as an ESAT-6:CFP-10 heterodimeric complex stabilized by two salt bridges. This is crucial for the secretion and the stability of ESAT-6 in the intracellular environment of the phagosomal lumen.[3] Native ESAT-6:CFP-10 heterodimers extracted from *Mtb* were found to dissociate under acidic pH; however, only ESAT-6 and not CFP-10 is known to interact with the phagosome membrane.[4] Purified recombinant ESAT-6 has been implicated in the lysis of artificial lipid membranes,[4] red blood cells,[5] and cultured macrophages through permeabilization of both the phagosome membrane and the cell membrane upon gaining access to the cytoplasm.[6–8] Purified ESAT-6, but not other ESX-1-secreted proteins, has been shown to induce pore formation in host cell membranes.[5,9,10] The membrane-interacting activity of ESAT-6 is known to largely depend on acidic-pH-dependent conformational changes *in vitro*.[9] It has also been reported that many of the pore-forming activities ascribed to ESAT-6 are due to the residual detergent contamination from ESAT-6 purification in widely used protocols.[11,12] ESAT-6 is found to induce significant deformation of non-acidified phagosomes. Yet under acidic conditions, the liposome membrane is known to undergo lysis induced by both the native and recombinant ESAT-6 in the absence of contaminating detergents.[13]

Interestingly, a recent study reported that ESAT-6 alone is not sufficient for phagosome disruption. Instead, direct bacterial physical contact was found to be important for gross phagosomal membrane disruption.[11] *In vivo* observations also suggest that ESAT-6 requires additional factors such as the lipid phthiocerol dimycocerosate for phagosomal disruption.[12,14,15] *Mycobacterium marinum* transposon mutants have also been found to be capable of phagosome damage despite their inability to secrete ESAT-6, hinting that ESAT-6 alone may not be sufficient for the ESX-1 virulence function.[16] However, there is also strong evidence supporting ESAT-6's direct role in phagosome lysis and virulence.[9,17,18] Most recently, the C terminus of ESAT-6 was shown to be required for phagosomal membrane damage.[13] Although the ability to damage the phagosomal membrane has emerged as central to *Mtb* virulence, the mechanism of ESAT-6-mediated phagosome membrane disruption remains poorly understood.[1] In particular, insights into the dynamics of ESAT-6 interaction and membrane remodeling of the phagosome are lacking.[2]

This work demonstrates that ESAT-6 undergoes fibrillation both *in vitro* and *in vivo*, disrupting the phagosome-like compartment through vesiculation. The binding of ESAT-6 to the membrane is shallow, remodeling the membrane into tubules and spherical buds in a concentration-dependent manner. However, bud fission is induced by ESAT-6 polymerization. Numerical simulations demonstrate that growing fibrils generate both radial and tangential forces remodeling the membrane. Further ESAT-6 binding triggers local changes in curvature and lipid phase separation on a membrane under tension because of forces generated by fibrils. Finally, vesiculation of the phagosome-like compartment occurs

due to increased membrane areal strain, inducing apoptosis and host cell death, potentially aiding infection.

Result

ESAT-6 induces tubular deformations in the phagosome-like compartment membrane via shallow insertion

Mtb blocks phagosomal maturation by secreting the virulence effector protein ESAT-6 through the ESX-1 secretion system. ESAT-6 is known to have a membranolytic activity that helps *Mtb* escape into the cytosol.[1,13] However, the mechanism of ESAT-6-mediated disruption of the phagosomal membrane remains unknown. The binding affinity of ESAT-6 on a phagosomal membrane mimic (40% 1,2-dioleoyl-*sn*-glycero-3-phosphocholine [DOPC], 5.5% 1,2-dioleoyl-*sn*-glycero-3-phosphoethanolamine [DOPE], 22% sphingomyelin (SM), and 32.5% cholesterol)[19] was quantified using the tryptophan intrinsic fluorescence of ESAT-6. Upon titration of 5 μM ESAT-6 with increasing lipid concentrations (ranging from 0 to 600 μM) using liposomes, we observed a concentration-dependent reduction in the fluorescence intensity of ESAT-6 tryptophan residues, hinting at a weak association with the membrane (i.e., membrane binding affinity, K_d ~400 μM (Figure 1B). This is in line with the recently reported rapid self-association of ESAT-6 as a result of its low dissociation constant (i.e., K_d ~1.5 μM).[20] The maximum tryptophan fluorescence of ESAT-6 was observed between 315 and 335 nm (Figure S1).

To visualize the dynamics of ESAT-6 interaction in real time, we first immobilized giant unilamellar vesicles (GUVs; 10–50 μm), mimicking phagosomal composition doped with 0.01% biotinylated polyethylene glycol (PEG) to facilitate conjugation to a streptavidin-passivated surface. The GUVs were labeled with 0.1% rhodamine-PE and incubated with 5 μM fluorescein isothiocyanate (FITC)-labeled recombinant mycobacterial ESAT-6 (see STAR Methods). Although this is topologically opposite, the micrometer scale of the phagosome-like compartment and the cell membrane will both have a zero mean curvature and thus appear planar for ESAT-6 of 10–20 Å width.[21] ESAT-6 homogeneously bound to the GUV surface within 10 s of protein injection, followed by tubular deformation of the immobilized GUVs within a minute (Figure 1C; Video S1; Figure S2; schematic representation in Figure 1A). Although fine tubular structures were observed on the GUV membrane surface upon the injection of ESAT-6, it is difficult to rule out the possibility that the observed structures arose due to the wide point spread function in the confocal imaging (Figures 1C and 1D). Visualizing protein-induced small tubular structures, particularly during their emergence, can be challenging as they are mostly below the optical resolution.[22,23] The superresolution image of the equatorial plane of the ESAT-6-bound GUV revealed discrete local binding and changes in curvature capturing the onset of membrane shape transition (Figure 1E). The diffusion of the membrane-bound ESAT-6 was found to only partially decrease as evident from significant fluorescence recovery after photobleaching, and the rate of diffusion was estimated to be 0.11 $\mu m^2/s$ (Figure 1F). To examine the ESAT-6 insertion in the membrane, we performed steady-state fluorescence using depth-sensing fluorescence-quenching probes 5-Doxyl-PC and 12-Doxyl-PC with a constant concentration of 10 mol %. Depth-sensitive fluorescence quenching allows

estimation of the depth of membrane penetration of a fluorophore attached to the target molecule with the quenchers attached at various depths of the membrane bilayer.[24,25] ESAT-6 has three tryptophan residues in its sequence that allowed us to monitor the fluorescence intensity of the tryptophans in the presence of the doxyl probes (Figure 1G). In contrast to the bilayer spanning model of pore formation,[4,5,10,26] we observed that as the concentrations of ESAT-6 increased, the 5-Doxyl-PC, which corresponds to a depth ~12 Å from the center of the bilayer, showed more quenching effect compared to the 12-Doxyl-PC. This suggests that ESAT-6 does not penetrate the entire bilayer; instead, it inserts only until C5 of the acyl chain in the interacting leaflet. We further observed that ESAT-6 has a preferential binding for the phosphatidylcholine (DOPC) head group. Among the reconstituted minimal lipid membranes of the phagosome-like compartment, the highest binding intensity was observed for the DOPC membrane, followed by the DOPC/sphingomyelin membrane. The presence of 30% cholesterol in the DOPC membrane results in the weakest binding of ESAT-6, hinting at the possible role of packing density in the binding of ESAT-6 (Figure 1H). Although the observed difference in binding intensities of ESAT-6 between individual lipid membranes is quite low, the phagosomal membrane showed many folds higher binding (Figure 1I).

ESAT-6 binding reduces the membrane tension and makes it more compressible

We further examined the fate of the cell membrane tension during ESAT-6-mediated remodeling. Phagosome membrane is derived from the cell membrane[27]; we thus monitored the fluorescence lifetime change in the cell membrane of cultured THP-1-differentiated macrophages treated with ESAT-6 over 10 min and doped with 100 nM Flipper-TR, a membrane tension sensor.[28,29] We found that binding of 5 μM ESAT-6 to the macrophage cell membrane results in a decrease in the fluorescence lifetime from 4.2 to 3.4 ns, indicating a significant reduction in the cell membrane tension (Figures 2A and 2C). It is reasonable to say that ESAT-6 interaction with the phagosomal membrane would also reduce the membrane tension. Indeed, the fluorescence lifetime of the tension sensor in the reconstituted GUVs mimicking phagosomal membrane decreased from 4.5 to 3.7 ns upon the interaction with 5 μM ESAT-6 (Figures 2B and 2C), suggesting a significant reduction in the tension, as previously reported for endosomes.[29]

We next examined the response to compression, in the plane of the membrane, upon the binding of ESAT-6 using lipid monolayer membranes. Langmuir monolayers enable the quantification of lateral lipid interactions and compressibility modulus.[30–32] The addition of 5 μM ESAT-6 in the buffered subphase equilibrated to 0 mN/m led to an increase in the surface pressure to 27 mN/m and stabilized over ~1 h, suggesting the surface-active and amphiphilic nature of ESAT-6 (Figure S3). In the presence of a phagosomal model lipid monolayer equilibrated at bilayer equivalence pressure of ~31 mN/m (i.e., bilayer equivalence range of 30–35 mN/m), the addition of ESAT-6 led to a rise in surface pressure up to ~33 mN/m over an hour, hinting at a weak interaction with membrane (Figure S4). We next examined the ESAT-6-induced changes in area per lipid molecule and phase behavior of the phagosomal model monolayer membrane. Analysis of the ESAT-6-bound phagosomal model membrane surface pressure (π)-area isotherm (A) revealed a plateau at 28–32 mN/m, suggesting the transition from a liquid-expanded (l_e) to a liquid-condensed (l_c) phase (Figure

2D). The compressibility modulus (C_s^{-1}) of the ESAT-6-bound membrane was extracted from the π-A isotherm using the following equation:

$$CS^{-1} = -A(d\pi/dA).$$

(Equation 1)

The C_s^{-1} of the monolayer at the bilayer equivalent surface pressure of ~30–35 mN/m is considered to be analogous to the elasticity of a bilayer membrane because the hydrophobic free energy and area per lipid are similar to those in a membrane bilayer at this pressure.[30,32,33] The C_s^{-1} of the phagosomal membrane decreased 2-fold from ~180 to ~90 mN/m upon the interaction of ESAT-6, suggesting the membrane is more compressible and, thus, easier to deform (Figure 2E).

Higher surface density of ESAT-6 induces phagosomal membrane budding and initiation of vesiculation

The physiological concentration of ESAT-6 inside the phagosome remains unknown; however, considering the confined volume of the phagosome, the local concentration of the secreted protein can be high. Thus, we used a range of concentration from 1 to 20 μM in line with the previous *in vivo* and *in vitro* studies that used concentrations ranging from 1 to 50 μM.[34–36] Considering the size of a phagosome to be on the order of 2–5 μm, the ratio of the available surface area and number of secreted protein molecules inside a confined volume should be very low. We questioned whether the rise in the phagosome membrane-bound surface density of ESAT-6 induces any further remodeling and shape deformation. To capture this in real time, we incubated 20 μM unlabeled ESAT-6 with the immobilized phagosomal membrane mimic GUVs labeled with 0.1% rhodamine-PE. Extrapolating the change in the area per lipid molecule of a monolayer membrane upon the binding of unlabeled ESAT-6 for a GUV surface, the surface density of the ESAT-6 was estimated to be ~74 $\times 10^4$ molecules bound on a GUV with a radius of 15 μm (Method S1). To establish the functional role of ESAT-6 binding, we opted not to use FITC-labeled ESAT-6 at higher concentrations to rule out any potential hindrance caused by the FITC molecule on protein binding. No deformations were observed when the membrane was treated with other proteins (i.e., 20 μM CFP-10 or BSA) as control treatments at high concentrations, ruling out the role of osmolarity changes as a result of protein flux and proving the specificity of ESAT-6 interaction (Figure 2F; Videos S2 and S3). Interestingly, time-lapse imaging revealed that ESAT-6 induces large membrane tubules and buds on the membrane having both positive and negative curvature (Figures 2G and 2H; Video S4). The equatorial plane of the ESAT-6-bound GUVs showed some seemingly detached vesicles; however, we think most are still connected with tubular necks that remained out of focus. Occasional vesiculation mediated by ESAT-6 crowding cannot be ruled out, as observed in the z stack, and such observation was not common. The buds remained attached even after 45 min of monitoring without undergoing any visible change (Figure 2I). Size distribution analysis revealed that most of the budded vesicle sizes were less than 3 μm, compared to the mother vesicle sizes of around 15–20 μm, in diameter (Figure S6). Although the observed size appears to be several folds higher than the intracellular scale, we think that the size

of the bud might scale with the area available on the mother vesicle and lead to a broad range of bud size as the mother vesicle loses area.[37] We speculate that, for a phagosome-like compartment of size ~2 μm, this might result in the formation of phagosome-like compartment buds much smaller in size, often making it challenging to visualize as well as demarcate from other vesicular compartments due to technical limitations.

Previous reports have shown that mycobacterial translocation from phagolysosomes or phagosomes into the cytoplasm, in a non-apoptotic cell, can take up to few hours to days and involves ESAT-6 secretion as well as direct contact of the bacteria.[6,11] We hypothesized that prior to the *Mtb* escape, ESAT-6-mediated remodeling should be reflected in the polarity of the phagosomal membrane interface. Fluorescence lifetime is known to be sensitive to changes in the local environmental polarity of the membrane.[38] We quantified the fluorescence lifetime of the tryptophan residues of ESAT-6, at 30 min and 24 h post-treatment, by incubating 1, 5, and 10 μM ESAT-6 concentrations with the phagosomal model membrane. The fluorescence lifetime of the tryptophan residues of ESAT-6 decreased around 24 h, but not at 30 min, suggesting an increase in the local polarity over time (Figures 2J; Figure S5). This decrease in the fluorescence lifetime could be due to the insertion of water molecules into the membrane. However, at higher concentrations of ESAT-6, the change in the fluorescence lifetime was less pronounced due to a relatively greater number of proteins on the membrane, which hinders the insertion of water molecules (Figure 2K).

ESAT-6 fibrillation drives the rate of vesiculation of the phagosomal membrane

Many of the bacterial secretory proteins have been speculated to possess amyloidogenic propensity.[39] Perplexed by the observation that the buds predominantly remain attached to the phagosomal membrane, we next examined ESAT-6 behavior in the presence of a phagosomal membrane interface for a longer duration of time. Thus, we first investigated whether ESAT-6 shows any fibrillation characteristics estimated through thioflavin T (ThT) fluorescence assay (Figure 3A). Surprisingly, we discovered that 20 μM ESAT-6 undergoes rapid fibrillation under the phagosomal acidic pH of ~5.5 without any visible nucleation or lag phase and reaches the equilibrium phase around ~24 h, unlike other fibrillating proteins that take much longer[40,41] (Figure 3A). The pH specificity of ESAT-6 aggregation is evident from the prolonged nucleation phase spanning ~50 h at pH 7.4 (Figure S7). Aggregated ESAT-6 structures were also visualized in solution via microscopy around ~24 h (Figure S11). In contrast, the presence of the phagosomal membrane interface leads to a significant slowdown of the ESAT-6 fibrillation kinetics as evident from the nucleation phase lasting around ~20 h. Subsequently, fibrillation began around ~20 h and reached equilibrium by ~35 h (Figure 3A). Certain lipids have been found to inhibit or retard the fibrillation kinetics of several amyloidogenic proteins,[42] which might explain the observed slowdown in fibrillation kinetics. Further, no fibrillation of CFP-10 was observed in solution or in the presence of membrane, confirming the specificity of ESAT-6 fibrillation (Figure S8). The presence of CFP-10 in the compartmental lumen did not have any significant effect on the fibrillation kinetics of ESAT-6 (data not shown), thus suggesting molecular crowding does not affect the specificity of ESAT-6. The fibrillation behavior of ESAT-6 led us to test whether the same can happen inside THP-1-derived macrophages

in the cellular environment. Indeed, upon incubating recombinant FITC-labeled ESAT-6 with THP-1-derived macrophages treated with NIT-OH (a red fluorescent dye specific for cell membrane), the ESAT-6 was phagocytosed (Figure 3B). Further, the phagocytosed ESAT-6 vesicles pinched off from the cell membrane, and the ESAT-6 intensity inside the phagosome-like compartment increased by 8-fold compared to the extracellular environment (Figure 3C). Such puncta are often related to the aggregated forms of the proteins, as reported earlier for ESAT-6 as well as other amyloidogenic proteins.[20,42,43] Subsequently, the phagosome-like compartment numbers decreased over a few hours, suggesting the disruption and cytosolic access of the ESAT-6 (Figure 3D). To rule out that the observed decrease in the fluorescence intensity was due to the phagolysosomal fusion, we performed a lysosomal leakage assay, which showed that there was no significant reduction in the fluorescence intensity of the LysoTracker up to 2.5 h of ESAT-6 incubation (Figure S9). A striking fibrillar network spanning the entire equatorial plane of the cell was visualized after 24 h via live-cell imaging through confocal as well as structured illumination microscopy (SIM), suggesting continued polymerization of the protein (Figure 3E). Further, to prove that ESAT-6-induced deformation and vesiculation result in the leakage of the ESAT-6 into the cytosol, we performed an *in vitro* leakage assay using 5,6-carboxyfluorescein that demonstrated leakage induced by ESAT-6 in a concentration-dependent manner (Figure S10).

We next captured the changes in the phagosomal membrane shape and fibril assembly at ultra-high-resolution at the end of the fibrillation phase (i.e., ~24 h) using reconstituted large unilamellar vesicles (LUVs). Negative-stain transmission electron microscopy (EM) revealed polymeric fibrillar structures of ESAT-6 both in the presence and in the absence of the phagosome-like compartment membrane interface. ESAT-6 fibrils in the absence of membrane seemed to have formed thicker bundles (Figure 3G). In comparison to the mother vesicle size ranging from 200 to 300 nm in diameter, most fields of view showed significantly smaller vesicles in the range of ~40–70 nm tangled with ESAT-6 fibrils (Figures 3H and 3I; Figure S13). The area of contact of fibrils with the membrane interfaces was found to be both radial and tangential (Figure 3I). Many of the captured vesicles also showed intact membrane bud necks in contact with the tip of the ESAT-6 fibrils. Quantification of the fibril length revealed most fibrils to be around ~400–800 nm in length (Figure S12). This led us to question whether the ESAT-6 polymerization on the vesicular membrane interfaces is essential for fission. To address this, we used dynamic light scattering to monitor the change in size of the mother vesicles in the presence of ESAT-6 over time. Monitoring the reaction containing 20 μM ESAT-6 and LUVs (~1 μm in diameter), mimicking the phagosomal membrane, revealed a significant peak shift from 1 μm to ~70–80 nm at 24 h (Figure 3J). In contrast, no significant change in the vesicle size was observed in the absence of ESAT-6 (Figure 3F). Furthermore, neither 1 nor 5 μM ESAT-6 induced any shift in vesicle size, suggesting no bud fission over the monitored period of 30 h (Figure 3J).

The ThT fluorescence kinetics of 1 and 5 μM ESAT-6 on the phagosomal model membrane indeed showed a long nucleation phase without any elongation phase, confirming the absence of fibrillation (Figure S8). This suggests that ESAT-6 fibrillation is essential for fission of the buds, and the kinetics of the fission are dependent on the fibrillation rate

that in turn depends on the concentration of the protein. We next wondered whether such budding and vesiculation might indeed happen in the phagosome-like compartment of THP-1-derived macrophages. Indeed, the ESAT-6 endocytosed compartment showed striking budded structures with the presence of dense polymeric structures lining the inner surface as well as spread all over the lumen of the compartment (Figures 4A–4C), unlike the untreated macrophages (Figure S14). The presence of ESAT-6 polymeric structures was confirmed by immunogold EM using hexa-His antibody staining against ESAT-6 (Figures 4D–4G). The inlays in the immunogold micrographs show the colocalization of ESAT-6 signal at the budded structures arising both inside and on the compartment (Figures 4E and 4G).

The shape transitions of phagosomal membrane deformations are driven by the polymerization forces of ESAT-6

We next examined the role of ESAT-6 fibrillation in inducing membrane deformation and fission. The polymerization of proteins such as actin and β-microglobulin has been reported to generate active forces in driving the transition of a flat membrane to a bud.[44,45] We used numerical simulations to capture the scaling between the force generated by a growing network of ESAT-6 fibrils and membrane shape. The polymerization of ESAT-6 results in the formation of fibrils with varying lengths (Figures 3G and 3H). These fibrils interconnect to create a mesh or a network-like structure typical of polymerizing proteins (Figures 3H and 3I). We find that one end of the fibril remains attached to the membrane either radially or tangentially (Figures 3H and 3I) and hypothesize that the polymerization at the other end exerts a ratcheting motion against the phagosomal membrane. This ratcheting effect generates forces that play a role in shaping the membrane.[34–36] To model the shape transition of the phagosomal membrane by the ESAT-6 network, we employ Helfrich formalism[46] to account for the curvature-mediated membrane energetics. We explicitly incorporate additional terms in the Helfrich free energy to account for the forces exerted by the fibrils. Helfrich free energy has been widely used to understand membrane surface deformation.[45,47–52]

In our model, the forces exerted by the fibrils include both vertical and radial components (Figure 5A). The deformed membrane is assumed to exhibit axis symmetry along the z direction (Figure 3I). Furthermore, we model the double-layered structure as a monolayered surface, serving as a plausible mimic of the phagosomal membrane. The total energy of the membrane (E) is defined as:

$$E = \int dA\left[2\kappa(C - C_0)^2\right] + \int dA\sigma + \int -dp\left(F_R r + F_Z z\right) f(r, \theta, z(r)) .$$

(Equation 2)

The first term in Equation 2 represents the Helfrich bending energy functional, where C stands for the mean curvature of the surface, C_0 for the intrinsic curvature, k for the bending rigidity, and dA for infinitesimal area element of the membrane. The second term defines the energy due to surface tension, where σ represents the surface tension of the membrane. The last term accounts for the energy due to forces exerted by ESAT-6 fibrils, where F_R

and F_Z represent the radial and vertical forces, respectively. In the last expression, $\boldsymbol{p} = (r, \theta, z(r))$ and $f(r, \theta, z(r)) = 1$ for the region of the membrane where the fibrillation force is acting; otherwise, $f(r, \theta, z(r)) = 0$.[45] We minimize the free energy of the system by numerically solving Equation 2 using Monte Carlo simulated annealing.[45,52] For details of the simulations, see Methods S2.

Because the binding of ESAT-6 in the phagosomal membrane is shallow, we expect that such binding would induce a localized intrinsic curvature at the binding sites. This leads to an observable deformation in the shape of the membrane (Figure S16). In addition, we expect that as the surface density of ESAT-6 increases, the number of membrane-bound ESAT-6 fibrils will also rise significantly, resulting in a higher degree of deformation. We chose the vertical and radial forces on the order of pN to mimic biological forces as has been measured for actin and other polymerizing protein networks.[34–36] Systematically applying vertical forces (F_Z) induces changes in the membrane shape, leading to a noticeable increase in the size of the tubular bud (Figures 5B–5E). Furthermore, when radial forces (F_R) are introduced, a distinct neck forms along with a spherical bud (Figures 5F–5I). This highlights the significance of both vertical (F_Z) and radial (F_R) forces in reshaping the deformed membrane. Specifically, the vertical force regulates the size of the bud, while the radial force governs the shape, leading to the formation of a constricted neck. Our theoretical analysis suggests that the primary driver of membrane deformation is the forces generated due to ESAT-6 fibrillation. The outcome of this force-induced effect is the formation of a tubular bud, transitioning into a spherical bud, accompanied by the development of a distinct neck. Importantly, this specific shape configuration is crucial for facilitating the subsequent fission process, where the spherical bud detaches from the neck. EM images (Figures 3H and 3I) show the cooccurrence of ESAT-6 fibrils meshed with the membrane and the corresponding deformation, thereby supporting our theory of fibrillation-driven membrane deformation. In addition, the mere presence of free-standing tubular necks without tension and strain did not undergo ESAT-6-mediated fission of the buds (Figure 4J), further establishing the role of fibrillation in fission. Furthermore, the ESAT-6 ΔN-terminal mutant retards the polymerization, whereas the ΔC-terminal mutant does not induce any polymerization (Figure 5K), resulting in slow vesiculation and no vesiculation, respectively (Figure 5L). Thus, it is strongly indicated that the polymerization force is essential.

ESAT-6 fibrils facilitate membrane fission by exerting forces that increase areal strain and induce local lipid sorting

To validate the observations from the numerical simulations, we subjected the membrane to stretching forces under equiosmolar conditions to rule out any potential osmotic issues. Capturing the force exerted on the membrane by the polymerizing ESAT-6 is technically limiting, as fibrillation starts only after a nucleation lag period of ~20 h *in vitro*. To circumvent this, a negative pressure of 50 Pa, which corresponds to 0.5 pN/μm^2, was applied to the phagosomal membrane GUV by micropipette aspiration to mimic the exerted polymerization forces. Biological forces generally operate on the order of pN, as has been measured for actin and other fast-polymerizing protein networks.[34–36] A stable aspirated tongue length was obtained in the case of the phagosomal membrane GUV that did not undergo any change in the tongue length for the monitored duration of ~5 min (Figure 6A;

Video S5). Upon the injection of the unlabeled monomeric/lower oligomeric ESAT-6, the aspirated tongue length gradually increased followed by an expanding lipid phase separation area in the middle of the tongue (Figure 6B; Video S6). Rhod-PE is known to preferentially partition into liquid disordered regions of the membrane, resulting in enhanced fluorescence intensity upon lipid segregation.[53,54] As a result, a high-curvature tubular neck formed in the middle of the tongue before fission. Upon fission of the tip of the tongue, the remaining tongue relaxed back to the GUV surface and retracted out of the micropipette. We then quantified the change in membrane tension induced by the ESAT-6 using Laplace's law (Equation 3):

$$\tau = \Delta p(R_p . R_v)/2(R_v - R_p), \quad \text{(Equation 3)}$$

where R_V is the radius of the vesicle and R_p is the protrusion radius. Furthermore, estimating the areal strain (i.e., area stretch modulus, $/a_0$) exerted by the ESAT-6 interaction on a phagosomal membrane under high membrane tension using the Equation 4,

$$\Delta a/a_0 = R_p^2(1 + L_p/R_p)/2R_v^2, \quad \text{(Equation 4)}$$

revealed that there is a 3-fold increase in the areal strain before the fission of the bud (Figure 6C; Video S6). Analysis of the relationship between change in tension and areal strain revealed that, while areal strain increased throughout the fission process, the membrane tension increased up to the constriction point followed by relaxation and attaining equilibrium after the vesiculation. The observed relative change in area of the vesicle as a result of ESAT-6 binding rules out any possibility of osmosis[55] (Figure 6D). We next questioned whether the observed lipid phase separation under high membrane tension is solely a consequence of stretching or whether it could also be induced by the biochemical exchange of material between the bacteria and the phagosomal membrane under physiological conditions.[56] Direct contact of the mycobacteria with the phagosomal membrane is also considered important for phagosomal rupture in addition to ESAT-6.[11] To address this in real time, we first reconstituted *in vitro* live GFP-*Mycobacterium smegmatis* encapsulated inside a phagosomal membrane GUV. The viability of the encapsulated bacteria was found to be 75% by estimating the colony-forming units by bacteria subjected to electroformation conditions (Figure S15). The encapsulated bacteria in direct contact likely induced surface adhesion of the GUV membrane lipids as evident from the merged fluorescence signal at the area of contact (Figure 6E). The direct contact also resulted in the local bending of the membrane captured in z stack (Figure 6F). In addition, a higher load of the encapsulated bacteria inside the phagosome-like compartment membrane GUV resulted in both shape deformation and significant lipid phase separation wherein the Rhod-PE was observed to preferentially enrich below the equatorial plane of the GUV (Figures 6G and 6H, time lapse and z stack). Reconstituting phagosome-like GUVs containing the lipids isolated from the mycobacterial cell envelope induced striking phase-separated domains as evident from the preferential partitioning of Rhod-PE (Figure 6J). The experiment explores

the scenario where the mycobacteria are in direct contact with the phagosomal membrane, thereby possibly engaging in lipid exchange and resulting in phase separation. This suggests that material exchange as a result of direct contact cannot be ruled out as one of the potential factors inducing phase separation.

The observed membrane vesiculation *in vitro* as well as the fibrillation of ESAT-6 inside macrophage cells then led us to question the fate of the homeostatic state of the cell. In line with the previous reports,[8,12,57,58] we observed that ESAT-6 induced a high rate of apoptosis as evident from Annexin V-propidium iodide (PI) staining in a concentration- and time-dependent manner, which correlates with the observed *in vitro* fibrillation kinetics of ESAT-6 (Figure 7A). The high-resolution EM captured significant morphological changes in the macrophages resulting in the disintegration of the nucleus and cell membrane rupture, which leads to the release of cellular contents when treated with 20 μM ESAT-6 and incubated for 24 h (Figures 7B and 7C). This suggests that after the vesiculation of the phagosomal membrane, ESAT-6 escapes into the cytosol and induces apoptosis leading to cell death.

Discussion

Phagosome disruption is one of the key aspects in the arrest of phagosome maturation and the egress of *Mycobacteria*.[2,59] It is reported that *Mtb* ruptures the phagosome membrane and escapes after 48 h through an ESAT-6-mediated phagosome lysis[6,7]; however, the molecular mechanism remains elusive.[2,11,13,59] ESAT-6 inserts in a membrane-spanning conformation that provides the foundation for pore formation based on hemolysis assay.[5,9,10] An important reason behind the observed membrane-spanning pore-forming conformation could be the usage of oversimplified lipid composition, that is, DOPC. The packing density arising due to the cylindrical geometry of the DOPC may facilitate the deep insertion of the ESAT-6[60] but might not be the case for a complex multicomponent biological membrane.[42] In contrast, we show that ESAT-6 inserts only until C5 of the acyl chain on a biologically relevant phagosomal membrane mimic comprising a lipid composition of complex geometry. Pore formation may occur transiently as an intermediate step, owing to weak binding to the membrane as confirmed by high K_d as well as diffusion (Figures 1B and 1F). Unlike the ESX-E/F secretory proteins and other pore-forming proteins, there is no concrete experimental evidence for pore formation by the oligomeric assembly of ESAT-6.[61–64] Indeed, the changes in the conductance pattern induced by ESAT-6 measured on artificial lipid bilayers suggest a non-uniform fluctuation and were speculated to be due to the amyloidogenic properties of ESAT-6 as also seen in some bacterial toxins.[26,39] ESAT-6 binding to membranes at low and high surface densities induced shape transition from slightly curved to tubular structures (Figures 1C and 1D) and membrane buds. The binding of the protein makes the phagosome-like compartment membrane more deformable, enabling the generation of curved protrusions as is evident from the reduction in the compressibility modulus and membrane tension (Figures 2E and 2A–2C). However, the buds do not detach from the GUV surface until after 24 h (Figures 2G and 2H). The observed tubulations and buds can be attributed to the changes in local membrane curvature and lateral pressure introduced as a result of high surface density and shallow insertion of ESAT-6 pushing away the lipid head groups in the interacting membrane leaflet.[65–68]

Indeed, the magnitude of the protein-induced membrane bending and curvature generation is known to non-monotonously depend on the insertion depth of the protein for biologically relevant conditions.[67,69] Shallow embedding of amphipathic helices induces formation of tubes of varying sizes.[70–72] Recently, tubulation and budding were reported in the phagolysosomes containing *E. coli* important for lysosomal re-formation during phagosome resolution.[73]

We then wondered why the detachment of the membrane buds takes around 24 h (Figure 2I). ESAT-6 is known to form amyloid-like structures in the inclusion bodies of *E. coli*, making the kinetics of transition much faster.[39] However, very recently ESAT-6 was reported to undergo rapid self-association, though lacking any evidence of fibrillation.[20] We provide the first evidence supporting fibrillation of ESAT-6 inside a macrophage phagosome-like compartment as well as in the cytosol upon leakage (Figures 3 and 4). The decrease in the number of phagosome-like compartments suggests that the kinetics of the disruption may vary *in vivo* and *in vitro*, depending on the local concentration of the protein. ESAT-6 fibrillates in the presence of a phagosome-like membrane interface that slows down the fibrillation kinetics and forms a mesh-like network at the equilibrium phase (Figures 3A–3C, 3H, and 3I). It is important to note that until the equilibrium phase is reached, ESAT-6 would exist as a mixture of monomers, oligomers, and fibrils, all of which can bind to the membrane with different affinities and deform the membrane.[42,43] Both the high surface density of the protein and the growing network of polymerizing protein are known to exert forces on the membranes resulting in local modulation of curvature and tension.[44,74–77] However, lowering the concentration of ESAT-6 or ΔC-terminal mutants showed no vesiculation, indicating that polymerization is essential for vesiculation. By keeping the membrane under elevated tension through aspiration to mimic the fibril-mediated force generation, the binding of oligomeric ESAT-6 triggers membrane fission accompanied by an increase in the membrane tension and areal strain (Figure 5B). This might be facilitated by both direct bacterial contact and curvature-driven lipid sorting aided by ESAT-6, as the phagosomal lipid composition is close to the demixing point.[78,79] We propose that the fibrillation of ESAT-6 inside the phagosome-like compartment might induce remodeling and/or vesiculation of the membrane, resulting in an alteration of the recruitment kinetics of various key endosomal markers essential for the maturation process. Further persistent vesiculation would decrease the surface area/volume ratio countering repair mechanisms, eventually inducing apoptosis as a result of stress. Together, these events might aid the mycobacterial escape and spread to other neighboring cells, promoting infection. The role of apoptosis during *Mtb* infection is debated[80–84]; however, by modulating the concentration of the secreted ESAT-6 inside the phagosome, *Mtb* may regulate its own residency time. The proposed mechanism explains the variation in the phagosomal escape time observed for *Mycobacteria* and could be crucial for pathogenesis.

Limitations of the study

The reconstituted system in this study is limited by the lack of compositional asymmetry of the phagosomal membrane leaflets and the Endosomal Sorting Complex Required for Transport (ESCRT) repair machinery. This might influence the timescales of the phagosome-like compartment disruption events that occur inside a phagosome versus a

Europe PMC Funders Author Manuscripts

cell-free reconstituted system. The endocytosed ESAT-6 concentrations inside the engulfed phagosome-like compartment might be different from the physiological concentration of ESAT-6 secreted by the engulfed *Mtb*, which remains unknown. However, the concentration regime used in this work should be physiologically feasible owing to the constitutive secretion of ESAT-6 inside the confined volume of the phagosome.

Resource Availability

Lead contact

Requests for further information and resources and reagents should be directed to and will be fulfilled by the lead contact, Mohammed Saleem (saleem@niser.ac.in).

Materials availability

This study did not generate any unique reagents. The plasmids used in this study are available upon request.

Star★Methods

Detailed methods are provided in the online version of this paper and include the following:

- KEY RESOURCES TABLE
- EXPERIMENTAL MODEL AND STUDY PARTICIPANT DETAILS
  - Mammalian cell culture
- METHOD DETAILS
  - Preparation of GUV
  - Overexpression and purification of ESAT-6 and ESAT-6 mutants
  - Fluorescence quenching assay
  - Light microscopy
  - 5(6)-carboxyfluorescein leakage assay
  - Lysotracker leakage assay
  - Fluorescence lifetime imaging (FLIM)
  - Time-resolved fluorescence measurements
  - Thioflavin T assay to determine kinetics of protein aggregation
  - Lipid monolayer experiments
  - Negative staining transmission electron microscopy
  - Thin section transmission electron microscopy
  - Immunoelectron microscopy (IEM)
  - Micropipette aspiration

- Subcellular fractionation and lipid extraction of mycobacterial cell envelope

- QUANTIFICATION & STATISTICAL ANALYSIS

Star⋆Methods

Key Resources Table

REAGENT or RESOURCE	SOURCE	IDENTIFIER
Antibodies		
Anti-His6-peroxidase (mouse monoclonal)	Sigma–Aldrich	Cat# A7058, RRID:AB_258326
Bacterial and virus strains		
E. coli BL21 (DE3, plysS) strain	This paper	N/A
Chemicals, peptides, and recombinant proteins		
1,2-dioleoyl-*sn*-glycero-3-phosphocholine (DOPC)	Avanti Polar Lipids	850375C
1,2-dioleoyl-*sn*-glycero-3-phosphoethanolamine (DOPE)	Avanti Polar Lipids	850725C
Brain SM	Avanti Polar Lipids	860062
di-stearoyl phosphatidyl ethanolamine-PEG (2000)-biotin	Avanti Polar Lipids	880129
Cholesterol	Avanti Polar Lipids	700000P
lissamine rhodamine B sulfonyl	Avanti Polar Lipids	810150C
Avidin	Sigma–Aldrich	A9275
FITC labelling KIT	Sigma–Aldrich	343210
Phosphate Buffer Saline	Sigma–Aldrich	P2272
isopropyl -D galactopyranoside	GOLD-BIO	12481C50
Nickel nitrilotriacetic acid (Ni-NTA) Resin	QIEGEN	30410
Triton-X	Himedia	MB031
Bovine serum albumin	MP BIOMEDICALS	162313
Lysotracker Red	Thermo	L12492
Flipper-Tr	Cytoskeleton	CY-SC020
Thioflavin T	Sigma–Aldrich	T3516
Glutaraldehyde	TED Pella	18420
Doxyl-5 PC	Avanti Polar Lipids	810601
Doxyl-12 PC	Avanti Polar Lipids	810600
Critical commercial assays		
Apoptosis Assay KIT	BD Pharmingen	559763
Oligonucleotides		
ESAT6 DELTA C FP 5‘-CATATGAC AGAGCAGCAGTGGAATTTCGCG-3‘	HKP Scientific	N/A
ESAT6 DELTA C RP 5‘-GAGCTCGA CGTTGCCTTCGGTCGAAGCCA-3‘	HKP Scientific	N/A
ESAT6 DELTA N FP 5‘-CATATGGGG AAGCAGTCCCTGACCAAGCTC-3‘	HKP Scientific	N/A
ESAT6 DELTA N RP 5‘-GAGCTCTGC GAACATCCCAGTGACGTTGCC-3‘	HKP Scientific	N/A

REAGENT or RESOURCE	SOURCE	IDENTIFIER
Software and algorithms		
SIGMAPLOT	Sigma plot software	N/A
IMAGE J	Image J Software	N/A
ORIGIN	National institute of science education and research, India	N/A
Python Simulation Code	GitHub Repository	https://github.com/Mintu-Nandi-24/Membrane-fission/tree/main

Experimental Model and Study Participant Details

Mammalian cell culture

The human monocytic THP-1 cell line was obtained from the National Collection of Authenticated Cell Cultures and cultured in RPMI 1640 medium (Thermo Fisher Scientific) supplemented with 10% fetal bovine serum (MP Biomedicals) and 20 μg/mL penicillin-streptomycin (Sigma-Aldrich). THP-1 cells were incubated overnight with 50 ng/mL phorbol 12-myristate 13-acetate (PMA, Sigma-Aldrich) to develop into adherent macrophages. All cells were cultured at 37°C in a 5% CO_2 humidified atmosphere. All cells used in this study are mycoplasma negative.

Method Details

Preparation of GUV

The phagosomal membrane mimic GUVs were composed of 40% DOPC, 5.5% DOPE, 22%BSM, 32.5% cholesterol, 0.03% PEG-Biotin, and 0.1% Rhod PE. To achieve a satisfactory yield of GUVs, the electroformation was performed as described in [23]. In summary, a uniform coat of 15μL of lipid mix at 5 mg ml^{-1} was first dried on conductive indium-tin oxide-coated glass (Nanion technologies, GmbH) under vacuum for at least 1 h. The lipid film was then rehydrated in a PBS (pH 5.5) at 300 ±5 mOsm and GUVs were allowed to grow for 3 h under a sine voltage (2V, 10 Hz) at 60°C. For encapsulation of the live Mycobacteria inside GUVs, the lipid film was rehydrated using 7H9 media with precultured Mycobacteria of OD 1-1.2.

Overexpression and purification of ESAT-6 and ESAT-6 mutants

E. coli BL21 (DE3, plysS) strain was utilized for the expression and purification of ESAT-6. The strain was transformed with the plasmid pET22b, which included the M. tb gene Rv3875 (protein ESAT-6). The transformed bacteria were grown in LB medium at 37 °C, and protein expression was done at OD600 nm~0.6, induced by adding 1 mM of isopropyl -D galactopyranoside (IPTG) overnight at 18 °C. Following, bacterial cells were pelleted, and sonicated, and the (His)6-tagged protein was purified using affinity chromatography with Nickel nitrilotriacetic acid (Ni-NTA) according to the manufacturer's recommendations (GE Healthcare, UK). SDS-PAGE analysis validated the purification of rESAT-6. The

purified fractions were dialyzed, concentrated, and kept in aliquots at -80 °C until further use.

The cloning and construction of ESAT-6 mutants were prepared using PCR based cloning. Primers for amplification and sequencing were mentioned earlier.

Fluorescence quenching assay

The interaction of ESAT-6 with the phagosomal membrane was observed through the intrinsic fluorescence of Tryptophan residue in ESAT-6. To measure the fluorescence intensity 5μM of ESAT-6 was equilibrated for 5 minutes with increasing lipid concentrations. The excitation wavelength was fixed at 290 nm and the emission spectra were collected between 300-400 nm at a constant temperature of 25 °C. All the fluorescence measurements were performed with an FLS 1000 (Edinburg Instruments, UK) spectrophotometer using a quartz cuvette with a 1cm path length.

Light microscopy

8 Well chamber slide from Ibidi was coated with 10μl of 1mg/ml streptavidin, and 200μL of biotinylated GUVs was added and incubated for 15 mins for the GUVs to be immobilized. The final concentration of 5μM of FITC-ESAT-6 was added into the chamber. Imaging was performed on Leica TCS SP8 LCSM using an appropriate laser for Rhodamine-PE (561nm) and Alexa-488 (488nm). Identical laser power and gain settings were used during all experiments.

For the Fluorescence recovery after photobleaching (FRAP) measurements on the GUVs, the GUVs were doped with 0.1% of rhodamine PE and were incubated with 5 μM of ESAT-6. Initially images were captured at reduced laser intensity. Photobleaching was performed at full laser intensity for 30 seconds, resulting in the bleaching within the selected ROI of radius of 5μm. Subsequently, the laser intensity was reverted to the attenuated level and the recovery curve was recorded.The photobleaching was performed at the equatorial plane of the GUV being visualized. The FRAP curves for each condition were repeated three times and then normalized. The diffusion coefficient was calculated using the Soumpasis equation for 2D diffusion

$$D_R = 0.224\frac{R^2}{\zeta_{1/2}}$$

(Equation 5)

where 0.244 is the numerically determined value, r (5 μm) stands for the radius of the laser beam focused on the region of interest, and $\tau 1/2$ is the time required for half the recovery. The time for half the recovery was determined by plotting the normalized recovery curve.

For the in-vivo experiments, the human monocyte cell line (THP-1) was incubated overnight with PMA along with the RPMI to differentiate into the macrophages. Cells were labeled with NIT-OH, a red fluorescent labelling dye. Followed by the treatment with the 20μM

Europe PMC Funders Author Manuscripts

FITC-ESAT-6 on the cells and super-resolution images were taken after 24 hours of incubation with the 488nm laser on Zeiss Elyra7.

5(6)-carboxyfluorescein leakage assay

The ESAT-6 induced Leakage was monitored using the 5(6)-carboxyfluorescein (CF) intensity as a function of time. The final monomeric ESAT-6 concentration was 20μM and 5μM was diluted in PBS solution (Ph-5.5) which comprises 200μM of LUV and 100mM of CF dye encapsulated inside the LUV. All the samples were incubated at 37°C in NUNC 96 well plate throughout the experiment. The plate was loaded into the 96-well Clariostar microplate reader equipped with 448/482-nm excitation/emission filters and the CF fluorescence intensity was monitored every 1 minutes of 30 cycles.

Lysotracker leakage assay

The Thp-1-derived macrophages were incubated with ESAT-6 for 2.5,2,1.5 and 1 hour respectively. Then, the cells were stained with Lysotracker Red (Thermofisher) for 30 min. After washing twice with PBS, the fluorescence intensity of the Lysotracker Red was quantified in the Clariostar microplate reader.

Fluorescence lifetime imaging (FLIM)

Fluorescence lifetime imaging microscopy was performed on an MT200 (Pico Quant, Berlin, Germany) time-resolved fluorescence confocal microscope with a Time-Correlated Single Photon Counting (TCSPC) unit. The laser power was adjusted between 10 to 100nW for 488nm laser light measured after the dichroic mirror. The Well glass bottom slide was directly placed on immersion water of 60x objective. A dichroic mirror of 488nm was used as the main beam splitter. Out-of-focus emission light was blocked by a 50 μm pinhole and the in-focus emission light was then split by a 50/50 beam splitter into two detection paths. Single Photon Avalanche Diodes (SPADs) served as detectors. Both data acquisition and analysis were performed on the commercially available software Sympho Time 64 (Pico Quant GmbH, Berlin, Germany).

Time-resolved fluorescence measurements

Time-resolved fluorescence intensity decays were obtained by using IBH 5000F Nano LED equipment (Horiba, Edison, NJ) in the time-correlated single photon counting (TCSPC) mode. The excitation source of a pulsed light-emitting diode (LED) was used. At 290nm optical pulses were generated by this LED with a pulse duration of 1.2 ns and emission was measured at 335nm with 1 MHz repetition rate. The Instrument Response Function (IRF) was quantified at the respective excitation wavelength using Ludox (colloidal silica) as a scatterer. 10,000 photon counts were collected in the peak channel to optimize the signal-to-noise ratio. The lifetime of tryptophan residue of ESAT-6 was performed using emission slits with a bandpass of 8 nm. Data were examined using DAS 6.2 software (Horiba, Edison, NJ). Fluorescence intensity decay curves were developed with the IRF and measured using:

Europe PMC Funders Author Manuscripts

$$F(t) = \sum_{i}^{n} \alpha_i \exp\left(-\frac{t}{\tau_i}\right)$$

All the plots were quantified with a random deviation of about zero with a maximum χ^2 value of 1.2 or less. Intensity averaged mean lifetimes τ_{avg} for fluorescence exponential decays were obtained from the decay times and pre-exponential factors using the following equation

$$\tau_{avg} = \frac{\sum \alpha_i \tau_i^2}{\sum \alpha_i \tau_i}$$

where α_I shows the fraction of τ_i lifetime.

Thioflavin T assay to determine kinetics of protein aggregation

The aggregation kinetics of ESAT-6 was monitored by ThT fluorescence as a function of time. The final monomeric ESAT-6 concentration was 20μM and 50μM was diluted in PBS solution (Ph-5.5) which comprises 200μM of LUV and 50μM of ThT dye. All the samples were incubated at 37°C in NUNC 96 well plate throughout the experiment. The plate was loaded into the 96-well Clariostar microplate reader equipped with 448/482-nm excitation/ emission filters and the ThT fluorescence intensity was monitored every 15 minutes of 500 cycles.

Lipid monolayer experiments

The monolayer experiments were performed in KSV NIMA Langmuir balance. The instrument consisted of two barriers used during the compression isotherms assays and as a surface pressure sensor a Wilhelmy microbalance with filter paper plate was used. Monolayers of DOPC: DOPE:SM: CHOL were formed by spreading the lipid/chloroform solution (1mg/ml) in a dropwise manner and kept for 15 mins to equilibrate the monolayers and for the evaporation of the chloroform. PBS (Ph-5.5) was used as the subphase with the maintained temperature of 25°C for all the Langmuir experiments. The final working concentration of 5μM ESAT-6 was injected into the monolayer for isotherm assays. Isotherms were recorded with uniform compression of the monolayer at a constant speed of 1 mm/min. Isotherms were recorded until collapse pressure (πc) was reached. For constant area assays (Time v/s surface Pressure), the monolayer is initially compressed to 30mN/m and allowed to equilibrate for 15 minutes. ESAT-6 was then injected into the subphase and the change in the surface pressure over time was recorded. For all the Langmuir experiments, the trough was cleaned thoroughly with ethanol and filtered double-deionized water until zero surface pressure was reached. Each experiment was performed thrice.

Negative staining transmission electron microscopy

10μl of the fibrillated ESAT-6 with LUVs was incubated in the carbon-coated grid for 20 minutes and wicked off with the help of qualitative filter paper from Himedia. Then 10μl of 2.5% glutaraldehyde was added to the grid for fixation of the sample. The carbon-coated grid was then rinsed using deionized water and 10μl of uranyl acetate was added. After

Europe PMC Funders Author Manuscripts

the incubation of 3 minutes and rinsing the grid with deionized water. The grid was then vacuum-dried overnight. The imaging was performed on a JEOL (JEM 2100F) transmission electron microscope.

Thin section transmission electron microscopy

For the cell-based experiments, ThP1-derived macrophages were treated with Esat-6 and incubated for 24 hours. Cells were washed with 0.1M phosphate buffer to get rid of cell culture media and processed for EM as described previously.[85] Briefly, cells were fixed with primary fixative (2.5% glutaraldehyde, 1.25% paraformaldehyde, and 0.1 M phosphate buffer, pH 7.0) for 15 min at RT. Cells were harvested and again resuspended in 1 ml fresh fixative media and incubated on ice for 1 hour. Cells were washed with 0.1M phosphate buffer followed by post-fixation with 1% osmium tetroxide (OsO_4) in 0.1 M phosphate buffer for 1 hour at RT followed by washing with distilled water twice. Next, cells were incubated with 1% uranyl acetate for 1 hour at RT. Subsequently, samples were dehydrated by incubating in increasing concentrations of ethanol (30%, 50%, 70%, 80%, 90%, 95%, and 100%) for 10 minutes each, with two more incubations in 100% ethanol from a freshly opened bottle. The samples were subsequently embedded stepwise using Spurr's low-viscosity resin (EMS). Samples were infiltrated for 2 h each with a 3:1, 1:1, 1:3 ethanol / embedding media mixture. Cells were incubated overnight with 100% fresh resin. The next day, cells were again resuspended in fresh 100% resin for 2–3 h, transferred into BEEM capsules (EMS), and polymerized at 70°C for 4 days. Semi- and ultrathin sections were produced with a diamond knife (Diatome) on an ultramicrotome (Ultracut UCT; Leica Microsystems), collected on 200 mesh copper grids (EMS), post-stained with uranyl acetate and lead citrate, and visualized with a Talos S200 transmission electron microscope (TEM; Thermo Fisher Scientific), operating at 200 kV. Pictures were recorded on a below-mounted 4k × 4k BM-Ceta (CMOS) camera.

Immunoelectron microscopy (IEM)

Immunoelectron microscopy (IEM) of cells was adapted as previously described (86). Briefly, cells were fixed with 0.1% glutaraldehyde and 4% paraformaldehyde for 2-3 hours. Fixed cells were completely dehydrated with ascending grades of alcohol (30%, 50%, 70%, 80%, 90%, 95%) followed by absolute alcohol. Further, cells were embedded by infiltration of LR white and polymerized at 65 ° C for 72 hours. 50-70 nm thin sections were mounted on the nickel grids. 2% skimmed milk were used for blocking and then grids were incubated with primary antibody anti-HIS (1:5) at 4 ° C overnight followed by incubation with gold conjugated secondary antibody (1:50) at room temperature. Samples were poststained with uranyl acetate and lead citrate and visualized with a Talos S200 transmission electron microscope (TEM; Thermo Fisher Scientific), operating at 200 kV. Pictures were recorded on a below-mounted 4k × 4k BM-Ceta (CMOS) camera.

Micropipette aspiration

All the measurements were performed on an Olympus IX83 epifluorescence microscope equipped with the Hoffman modulation optics and observed on the 100X objective lens. For positioning the pipette three-axis hydraulic micro-manipulators are used. Micropipettes are pulled (Sutter Instruments CO P-87, Narishige Micro forge MF-900) from 10μm diameter

Europe PMC Funders Author Manuscripts

capillaries. 100 μl of GUVs were added to the open homemade coverslip. The desired suction pressure for aspirating a GUV is provided, causing the vesicle to be aspirated through the micropipette tip and develop an inner protrusion. Over the period video was recorded to determine the vesicle geometry on the addition of the ESAT-6.

Subcellular fractionation and lipid extraction of mycobacterial cell envelope

The *M. smegmatis* were grown in 7H9 broth under continuous shaking for 3 days at 37° C. For subcellular fractionation, the culture was centrifuged at 4400g to obtain the bacterial pellet and carried out following the procedure outlined in[86] Briefly, the bacterial pellet was subjected to mechanical disruption twice using a French press followed by the bead beater by using microbeads (Himedia) to break the cells. Furthermore, the cells were lysed 2-3 times with beads and then centrifuged at low spin to remove unbroken cells. The supernatant was centrifuged 3-5 times at 27000g for 40 minutes to pellet the cell wall. The supernatant obtained previously was then ultracentrifuged at 100,000×g for 1 hour to obtain the cell membrane in the pellet fraction. Finally, the cell wall and cell membrane fractions were resuspended in PBS at a 1:1 ratio and stored in aliquots at -80°C.

Lipid extraction from the mycobacterial cell envelope was done by using the Folch method as described in[87]. The cell envelope was dried with nitrogen gas and kept in a vacuum overnight. The dried cell envelope was mixed with chloroform and then sonicated for 30 minutes at a constant pulse. The solution was again dried and chloroform and ice-cold methanol were subsequently added to the 2:1(V/V) ratio to the sample. After incubation in ice for 20 minutes same amount of distilled water was added as methanol and kept in ice for 10 minutes followed by centrifugation at 1500rpm for 5 minutes to separate the upper polar part containing salt and proteins and the lower organic phase containing lipids. The lower organic phase was dried using nitrogen gas and stored at -80°C.

Quantification & Statistical Analysis

The ImageJ software was used to analyze and process images. The fluorescent intensity plots along the equatorial plane of GUVs were quantified using the average fluorescence intensity of the membrane ($F_{vesicle}$) by subtracting the background intensity ($F_{background}$). A uniform detection setting was applied for all sets of experiments. Vesicle sizes were quantified manually using ImageJ. Statistical significance was calculated through one-way ANOVA in sigmaplot where p-values less than 0.05 were considered statistically significant throughout all the experiments.

Supplementary Material

Refer to Web version on PubMed Central for supplementary material.

Acknowledgments

We thank Thierry Soldati for critical comments on the manuscript. We thank Rohan Dhiman for the kind gift of the ESAT-6, CFP-10 plasmid, GFP-*M. smegmatis* strain, and THP-1 cell line. We thank Subhasis Chattopadhyay for his assistance with the flow cytometry. We thank Abdur Rahaman for the hexa-His antibody and Apurba Koner for the NIT-OH dye. We thank Ekta Tyagi for help during the molecular cloning. M.S. acknowledges

the DBT-Wellcome Trust India Alliance Intermediate Fellowship (grant IA/I/20/2/505212), Department of Atomic Energy, and SERB, India, for the National Post Doctoral Fellowship to M.N. (PDF/2022/001807).

Data and code availability

- All data reported in this paper will be shared by the lead contact upon request.
- The code for the Monte Carlo simulation used in this study is publicly available on GitHub (https://github.com/Mintu-Nandi-24/Membranefission/tree/main).
- Any additional information required to reanalyze the data reported in this paper is available upon request.

References

1. Bussi C, Gutierrez MG. Mycobacterium tuberculosis infection of host cells in space and time. FEMS Microbiol Rev. 2019; 43: 341–361. DOI: 10.1093/femsre/fuz006 [PubMed: 30916769]
2. Gröschel MI, Sayes F, Simeone R, Majlessi L, Brosch R. ESX secretion systems: mycobacterial evolution to counter host immunity. Nat Rev Microbiol. 2016; 14: 677–691. [PubMed: 27665717]
3. Renshaw PS, Lightbody KL, Veverka V, Muskett FW, Kelly G, Frenkiel TA, Gordon SV, Hewinson RG, Burke B, Norman J, et al. Structure and function of the complex formed by the tuberculosis virulence factors CFP-10 and ESAT-6. The EMBO journal. 2005; 24: 2491–2498. DOI: 10.1038/sj.emboj.7600732 [PubMed: 15973432]
4. De Jonge MI, Pehau-Arnaudet G, Fretz MM, Romain F, Bottai D, Brodin P, Honoré N, Marchal G, Jiskoot W, England P, et al. ESAT-6 from Mycobacterium tuberculosis dissociates from its putative chaperone CFP-10 under acidic conditions and exhibits membranelysing activity. J Bacteriol. 2007; 189: 6028–6034. DOI: 10.1128/JB.00469-07 [PubMed: 17557817]
5. Smith J, Manoranjan J, Pan M, Bohsali A, Xu J, Liu J, McDonald KL, Szyk A, LaRonde-LeBlanc N, Gao LY. Evidence for pore formation in host cell membranes by ESX-1-secreted ESAT-6 and its role in Mycobacterium marinum escape from the vacuole. Infect Immun. 2008; 76: 5478–5487. DOI: 10.1128/IAI.00614-08 [PubMed: 18852239]
6. van der Wel N, Hava D, Houben D, Fluitsma D, van Zon M, Pierson J, Brenner M, Peters PJ. M. tuberculosis and M leprae translocate from the phagolysosome to the cytosol in myeloid cells. Cell. 2007; 129: 1287–1298. [PubMed: 17604718]
7. Houben D, Demangel C, van Ingen J, Perez J, Baldeón L, Abdallah AM, Caleechurn L, Bottai D, van Zon M, de Punder K, et al. ESX-1-mediated translocation to the cytosol controls virulence of mycobacteria. Cell Microbiol. 2012; 14: 1287–1298. [PubMed: 22524898]
8. Simeone R, Bobard A, Lippmann J, Bitter W, Majlessi L, Brosch R, Enninga J. Phagosomal rupture by Mycobacterium tuberculosis results in toxicity and host cell death. PLoS Pathog. 2012; 8 e1002507 doi: 10.1371/journal.ppat.1002507 [PubMed: 22319448]
9. De Leon J, Jiang G, Ma Y, Rubin E, Fortune S, Sun J. Mycobacterium tuberculosis ESAT-6 exhibits a unique membrane-interacting activity that is not found in its ortholog from non-pathogenic Mycobacterium smegmatis. J Biol Chem. 2012; 287: 44184–44191. DOI: 10.1074/jbc.M112.420869 [PubMed: 23150662]
10. Ma Y, Keil V, Sun J. Characterization of Mycobacterium tuberculosis EsxA membrane insertion: roles of N-and C-terminal flexible arms and central helix-turn-helix motif. J Biol Chem. 2015; 290: 7314–7322. DOI: 10.1074/jbc.M114.622076 [PubMed: 25645924]
11. Conrad WH, Osman MM, Shanahan JK, Chu F, Takaki KK, Cameron J, Hopkinson-Woolley D, Brosch R, Ramakrishnan L. Mycobacterial ESX-1 secretion system mediates host cell lysis through bacterium contact-dependent gross membrane disruptions. Proc Natl Acad Sci USA. 2017; 114: 1371–1376. DOI: 10.1073/pnas.1620133114 [PubMed: 28119503]
12. Augenstreich J, Arbues A, Simeone R, Haanappel E, Wegener A, Sayes F, Le Chevalier F, Chalut C, Malaga W, Guilhot C, et al. ESX-1 and phthiocerol dimycocerosates of Mycobacterium tuberculosis act in concert to cause phagosomal rupture and host cell apoptosis. Cell Microbiol. 2017; 19 e12726 [PubMed: 28095608]

13. Osman MM, Shanahan JK, Chu F, Takaki KK, Pinckert ML, Pagán AJ, Brosch R, Conrad WH, Ramakrishnan L. The C terminus of the mycobacterium ESX-1 secretion system substrate ESAT-6 is required for phagosomal membrane damage and virulence. Proc Natl Acad Sci USA. 2022; 119 e2122161119 doi: 10.1073/pnas.2122161119 [PubMed: 35271388]

14. Barczak AK, Avraham R, Singh S, Luo SS, Zhang WR, Bray MA, Hinman AE, Thompson M, Nietupski RM, Golas A, et al. Systematic, multiparametric analysis of Mycobacterium tuberculosis intracellular infection offers insight into coordinated virulence. PLoS Pathog. 2017; 13 e1006363 doi: 10.1371/journal.ppat.1006363 [PubMed: 28505176]

15. Astarie-Dequeker C, Le Guyader L, Malaga W, Seaphanh FK, Chalut C, Lopez A, Guilhot C. Phthiocerol dimycocerosates of M. tuberculosis participate in macrophage invasion by inducing changes in the organization of plasma membrane lipids. PLoS Pathog. 2009; 5 e1000289 doi: 10.1371/journal.ppat.1000289 [PubMed: 19197369]

16. Lienard J, Nobs E, Lovins V, Movert E, Valfridsson C, Carlsson F. The *Mycobacterium marinum* ESX-1 system mediates phagosomal permeabilization and type I interferon production via separable mechanisms. Proc Natl Acad Sci USA. 2020; 117: 1160–1166. DOI: 10.1073/pnas.1911646117 [PubMed: 31879349]

17. Kennedy GM, Hooley GC, Champion MM, Medie Mba, Champion PAD. A novel ESX-1 locus reveals that surface-associated ESX-1 substrates mediate virulence in Mycobacterium marinum. J Bacteriol. 2014; 196: 1877–1888. DOI: 10.1128/JB.01502-14 [PubMed: 24610712]

18. Raffetseder J, Iakobachvili N, Loitto V, Peters PJ, Lerm M. Retention of EsxA in the capsule-like layer of Mycobacterium tuberculosis is associated with cytotoxicity and is counteracted by lung surfactant. Infect Immun. 2019; 87: 10–1128. DOI: 10.1128/IAI.00803-18 [PubMed: 30602503]

19. Ingólfsson HI, Carpenter TS, Bhatia H, Bremer PT, Marrink SJ, Lightstone FC. Computational lipidomics of the neuronal plasma membrane. Biophys J. 2017; 113: 2271–2280. DOI: 10.1016/j.bpj.2017.10.017 [PubMed: 29113676]

20. Bates TA, Trank-Greene M, Nguyenla X, Anastas A, Gurmessa SK, Merutka IR, Dixon SD, Shumate A, Groncki AR, Parson MA, Ingram JR. ESAT-6 undergoes self-association at phagosomal pH and an ESAT-6-specific nanobody restricts M. tuberculosis growth in macrophages. Elife. 2024; 12 RP91930 doi: 10.7554/eLife.91930 [PubMed: 38805257]

21. Bertin A, de Franceschi N, de la Mora E, Maity S, Alqabandi M, Miguet N, di Cicco A, Roos WH, Mangenot S, Weissenhorn W, Bassereau P. Human ESCRT-III polymers assemble on positively curved membranes and induce helical membrane tube formation. Nat Commun. 2020; 11: 2663. doi: 10.1038/s41467-020-16368-5 [PubMed: 32471988]

22. Mim C, Cui H, Gawronski-Salerno JA, Frost A, Lyman E, Voth GA, Unger VM. Structural basis of membrane bending by the N-BAR protein endophilin. Cell. 2012; 149: 137–145. DOI: 10.1016/j.cell.2012.01.048 [PubMed: 22464326]

23. Saleem M, Morlot S, Hohendahl A, Manzi J, Lenz M, Roux A. A balance between membrane elasticity and polymerization energy sets the shape of spherical clathrin coats. Nat Commun. 2015; 6: 6249. doi: 10.1038/ncomms7249 [PubMed: 25695735]

24. Muraoka T, Noguchi D, Kasai RS, Sato K, Sasaki R, Tabata KV, Ekimoto T, Ikeguchi M, Kamagata K, Hoshino N, et al. A synthetic ion channel with anisotropic ligand response. Nat Commun. 2020; 11: 2924. doi: 10.1038/s41467-020-16770-z [PubMed: 32522996]

25. Dijkman PM, Muñoz-García JC, Lavington SR, Kumagai PS, Reis Dos, Yin D, Stansfeld PJ, Costa-Filho AJ, Watts A. Conformational dynamics of a G protein–coupled receptor helix 8 in lipid membranes. Sci Adv. 2020; 6 eaav8207 doi: 10.1126/sciadv.aav8207 [PubMed: 32851152]

26. Hsu T, Hingley-Wilson SM, Chen B, Chen M, Dai AZ, Morin PM, Marks CB, Padiyar J, Goulding C, Gingery M, et al. The primary mechanism of attenuation of bacillus Calmette-Guerin is a loss of secreted lytic function required for invasion of lung interstitial tissue. Proc Natl Acad Sci USA. 2003; 100: 12420–12425. DOI: 10.1073/pnas.1635213100 [PubMed: 14557547]

27. Gotthardt D, Warnatz HJ, Henschel O, Brückert F, Schleicher M, Soldati T. High-resolution dissection of phagosome maturation reveals distinct membrane trafficking phases. Mol Biol Cell. 2002; 13: 3508–3520. DOI: 10.1091/mbc.E02-04-0206 [PubMed: 12388753]

28. Colom A, Derivery E, Soleimanpour S, Tomba C, Molin MD, Sakai N, González-Gaitán M, Matile S, Roux A. A fluorescent membrane tension probe. Nat Chem. 2018; 10: 1118–1125. DOI: 10.1038/s41557-018-0127-3 [PubMed: 30150727]

29. Mercier V, Larios J, Molinard G, Goujon A, Matile S, Gruenberg J, Roux A. Endosomal membrane tension regulates ESCRT-III-dependent intra-lumenal vesicle formation. Nat Cell Biol. 2020; 22: 947–959. DOI: 10.1038/s41556-020-0546-4 [PubMed: 32753669]
30. Brockman H. Lipid monolayers: why use half a membrane to characterize protein-membrane interactions? Curr. Opin Struct Biol. 1999; 9: 438–443. [PubMed: 10449364]
31. Yang S-T, Kiessling V, Tamm LK. Line tension at lipid phase boundaries as driving force for HIV fusion peptide-mediated fusion. Nat Commun. 2016; 7 11401 doi: 10.1038/ncomms11401 [PubMed: 27113279]
32. Nitenberg M, Bénarouche A, Maniti O, Marion E, Marsollier L, Géan J, Dufourc EJ, Cavalier JF, Canaan S, Girard-Egrot AP. The potent effect of mycolactone on lipid membranes. PLoS Pathog. 2018; 14 e1006814 doi: 10.1371/journal.ppat.1006814 [PubMed: 29320578]
33. Marsh D. Elastic curvature constants of lipid monolayers and bilayers. Chem Phys Lipids. 2006; 144: 146–159. [PubMed: 17045578]
34. Courtemanche N, Lee JY, Pollard TD, Greene EC. Tension modulates actin filament polymerization mediated by formin and profilin. Proc Natl Acad Sci USA. 2013; 110: 9752–9757. DOI: 10.1073/pnas.1308257110 [PubMed: 23716666]
35. Yu M, Yuan X, Lu C, Le S, Kawamura R, Efremov AK, Zhao Z, Kozlov MM, Sheetz M, Bershadsky A, Yan J. mDia1 senses both force and torque during F-actin filament polymerization. Nat Commun. 2017; 8: 1650. doi: 10.1038/s41467-017-01745-4 [PubMed: 29162803]
36. Yu M, Le S, Efremov AK, Zeng X, Bershadsky A, Yan J. Effects of Mechanical Stimuli on Profilin- and Formin-Mediated Actin Polymerization. Nano Lett. 2018; 18: 5239–5247. [PubMed: 29976069]
37. Lipowsky R. Remodeling of membrane shape and topology by curvature elasticity and membrane tension. Adv Biol. 2022; 6 2101020 [PubMed: 34859961]
38. Berezin MY, Achilefu S. Fluorescence lifetime measurements and biological imaging. Chem Rev. 2010; 110: 2641–2684. DOI: 10.1021/cr900343z [PubMed: 20356094]
39. Wang L, Maji SK, Sawaya MR, Eisenberg D, Riek R. Bacterial inclusion bodies contain amyloid-like structure. PLoS Biol. 2008; 6: e195. doi: 10.1371/journal.pbio.0060195 [PubMed: 18684013]
40. McGlinchey RP, Ni X, Shadish JA, Jiang J, Lee JC. The N terminus of ±-synuclein dictates fibril formation. Proc Natl Acad Sci USA. 2021; 118 e2023487118 doi: 10.1073/pnas.2023487118 [PubMed: 34452994]
41. Despres C, Byrne C, Qi H, Cantrelle FX, Huvent I, Chambraud B, Baulieu EE, Jacquot Y, Landrieu I, Lippens G, Smet-Nocca C. Identification of the Tau phosphorylation pattern that drives its aggregation. Proc Natl Acad Sci USA. 2017; 114: 9080–9085. DOI: 10.1073/pnas.1708448114 [PubMed: 28784767]
42. Tiwari A, Pradhan S, Sannigrahi A, Mahakud AK, Jha S, Chattopadhyay K, Biswas M, Saleem M. Interplay of lipid head group and packing defects in driving amyloid-beta–mediated myelin-like model membrane deformation. J Biol Chem. 2023; 299 104653 doi: 10.1016/j.jbc.2023.104653 [PubMed: 36990217]
43. Rose K, Jepson T, Shukla S, Maya-Romero A, Kampmann M, Xu K, Hurley JH. Tau fibrils induce nanoscale membrane damage and nucleate cytosolic tau at lysosomes. Proc Natl Acad Sci USA. 2024; 121 e2315690121 doi: 10.1073/pnas.2315690121 [PubMed: 38781206]
44. Shin W, Zucker B, Kundu N, Lee SH, Shi B, Chan CY, Guo X, Harrison JT, Turechek JM, Hinshaw JE, et al. Molecular mechanics underlying flat-to-round membrane budding in live secretory cells. Nat Commun. 2022; 13: 3697. doi: 10.1038/s41467-022-31286-4 [PubMed: 35760780]
45. Zhang T, Sknepnek R, Bowick MJ, Schwarz JM. On the modeling of endocytosis in yeast. Biophys J. 2015; 108: 508–519. DOI: 10.1016/j.bpj.2014.11.3481 [PubMed: 25650919]
46. Helfrich W. Elastic properties of lipid bilayers: theory and possible experiments. Z Naturforsch C Biosci. 1973; 28: 693–703. [PubMed: 4273690]
47. Kozlovsky Y, Kozlov MM. Membrane fission: model for intermediate structures. Biophys J. 2003; 85: 85–96. DOI: 10.1016/S0006-3495(03)74457-9 [PubMed: 12829467]
48. Kozlov MM. Fission of biological membranes: interplay between dynamin and lipids. Traffic. 2001; 2: 51–65. [PubMed: 11208168]

49. Alimohamadi H, Rangamani P. Modeling membrane curvature generation due to membrane–protein interactions. Biomolecules. 2018; 8: 120. doi: 10.3390/biom8040120 [PubMed: 30360496]
50. Hassinger J, Oster G, Drubin D, Rangamani P. Design principles for robust vesiculation in clathrin-mediated endocytosis. Biophys J. 2017; 112: 310a. doi: 10.1073/pnas.1617705114 [PubMed: 28126722]
51. Rangamani P, Mandadap KK, Oster G. Protein-induced membrane curvature alters local membrane tension. Biophys J. 2014; 107: 751–762. DOI: 10.1016/j.bpj.2014.06.010 [PubMed: 25099814]
52. Fošnarič M, Penič S, Iglič A, Kralj-Iglič V, Drab M, Gov NS. Theoretical study of vesicle shapes driven by coupling curved proteins and active cytoskeletal forces. Soft Matter. 2019; 15: 5319–5330. [PubMed: 31237259]
53. Baumgart T, Hammond AT, Sengupta P, Hess ST, Holowka DA, Baird BA, Webb WW. Large-scale fluid/fluid phase separation of proteins and lipids in giant plasma membrane vesicles. Proc Natl Acad Sci USA. 2007; 104: 3165–3170. DOI: 10.1073/pnas.0611357104 [PubMed: 17360623]
54. Baumgart T, Hunt G, Farkas ER, Webb WW, Feigenson GW. Fluorescence probe partitioning between Lo/Ld phases in lipid membranes. Biochim Biophys ActaCellule. 2007; 1768: 2182–2194. DOI: 10.1016/j.bbamem.2007.05.012 [PubMed: 17588529]
55. Shi Z, Baumgart T. Membrane tension and peripheral protein density mediate membrane shape transitions. Nat Commun. 2015; 6: 5974. doi: 10.1038/ncomms6974 [PubMed: 25569184]
56. Lerner TR, Queval CJ, Fearns A, Repnik U, Griffiths G, Gutierrez MG. Phthiocerol dimycocerosates promote access to the cytosol and intracellular burden of Mycobacterium tuberculosis in lymphatic endothelial cells. BMC Biol. 2018; 16: 1–13. DOI: 10.1186/s12915-017-0471-6 [PubMed: 29325545]
57. Behura A, Mishra A, Chugh S, Mawatwal S, Kumar A, Manna D, Mishra A, Singh R, Dhiman R. ESAT-6 modulates Calcimycin-induced autophagy through microRNA-30a in mycobacteria infected macrophages. J Infect. 2019; 79: 139–152. [PubMed: 31181223]
58. Lin J, Chang Q, Dai X, Liu D, Jiang Y, Dai Y. Early secreted antigenic target of 6-kDa of Mycobacterium tuberculosis promotes caspase-9/caspase-3-mediated apoptosis in macrophages. Mol Cell Biochem. 2019; 457: 179–189. [PubMed: 30911956]
59. Simeone R, Sayes F, Lawarée E, Brosch R. Breaching the phagosome, the case of the tuberculosis agent. Cell Microbiol. 2021; 23 e13344 [PubMed: 33860624]
60. McMahon HT, Boucrot E. Membrane curvature at a glance. J Cell Sci. 2015; 128: 1065–1070. DOI: 10.1242/jcs.114454 [PubMed: 25774051]
61. Tak U, Dokland T, Niederweis M. Pore-forming Esx proteins mediate toxin secretion by Mycobacterium tuberculosis. Nat Commun. 2021; 12: 394. doi: 10.1038/s41467-020-20533-1 [PubMed: 33452244]
62. Mulvihill E, Sborgi L, Mari SA, Pfreundschuh M, Hiller S, Müller DJ. Mechanism of membrane pore formation by human gasdermin-D. EMBO J. 2018; 37 e98321 doi: 10.15252/embj.201798321 [PubMed: 29898893]
63. Yu X, Ni T, Munson G, Zhang P, Gilbert RJC. Cryo-EM structures of perforin-2 in isolation and assembled on a membrane suggest a mechanism for pore formation. EMBO J. 2022; 41 e111857 doi: 10.15252/embj.2022111857 [PubMed: 36245269]
64. Sborgi L, Rühl S, Mulvihill E, Pipercevic J, Heilig R, Stahlberg H, Farady CJ, Müller DJ, Broz P, Hiller S. GSDMD membrane pore formation constitutes the mechanism of pyroptotic cell death. EMBO J. 2016; 35: 1766–1778. DOI: 10.15252/embj.201694696 [PubMed: 27418190]
65. Sheetz MP, Singer SJ. Biological membranes as bilayer couples. A molecular mechanism of drug-erythrocyte interactions. Proc Natl Acad Sci USA. 1974; 71: 4457–4461. DOI: 10.1073/pnas.71.11.4457 [PubMed: 4530994]
66. Roux A. Common principles of surface deformation in biology. Faraday Discuss. 2021; 232: 347–357. [PubMed: 34854444]
67. Campelo F, McMahon HT, Kozlov MM. The hydrophobic insertion mechanism of membrane curvature generation by proteins. Biophys J. 2008; 95: 2325–2339. DOI: 10.1529/biophysj.108.133173 [PubMed: 18515373]

68. Stachowiak JC, Schmid EM, Ryan CJ, Ann HS, Sasaki DY, Sherman MB, Geissler PL, Fletcher DA, Hayden CC. Membrane bending by protein–protein crowding. Nat Cell Biol. 2012; 14: 944–949. [PubMed: 22902598]
69. Simunovic M, Voth GA, Callan-Jones A, Bassereau P. When physics takes over: BAR proteins and membrane curvature. Trends Cell Biol. 2015; 25: 780–792. DOI: 10.1016/j.tcb.2015.09.005 [PubMed: 26519988]
70. Ford MGJ, Mills IG, Peter BJ, Vallis Y, Praefcke GJK, Evans PR, McMahon HT. Curvature of clathrin-coated pits driven by epsin. Nature. 2002; 419: 361–366. [PubMed: 12353027]
71. Martens S, Kozlov MM, McMahon HT. How synaptotagmin promotes membrane fusion. Science. 2007; 316: 1205–1208. [PubMed: 17478680]
72. Peter BJ, Kent HM, Mills IG, Vallis Y, Butler PJG, Evans PR, McMahon HT. BAR domains as sensors of membrane curvature: the amphiphysin BAR structure. Science. 2004; 303: 495–499. [PubMed: 14645856]
73. Lancaster CE, Fountain A, Dayam RM, Somerville E, Sheth J, Jacobelli V, Somerville A, Terebiznik MR, Botelho RJ. Phagosome resolution regenerates lysosomes and maintains the degradative capacity in phagocytes. J Cell Biol. 2021; 220 e202005072 doi: 10.1083/jcb.202005072 [PubMed: 34180943]
74. Engel MFM, Khemtémourian L, Kleijer CC, Meeldijk HJD, Jacobs J, Verkleij AJ, de Kruijff B, Killian JA, Höppener JWM. Membrane damage by human islet amyloid polypeptide through fibril growth at the membrane. Proc Natl Acad Sci USA. 2008; 105: 6033–6038. DOI: 10.1073/pnas.0708354105 [PubMed: 18408164]
75. Milanesi L, Sheynis T, Xue WF, Orlova EV, Hellewell AL, Jelinek R, Hewitt EW, Radford SE, Saibil HR. Direct three-dimensional visualization of membrane disruption by amyloid fibrils. Proc Natl Acad Sci USA. 2012; 109: 20455–20460. DOI: 10.1073/pnas.1206325109 [PubMed: 23184970]
76. Chiaruttini N, Redondo-Morata L, Colom A, Humbert F, Lenz M, Scheuring S, Roux A. Relaxation of loaded ESCRT-III spiral springs drives membrane deformation. Cellule. 2015; 163: 866–879. DOI: 10.1016/j.cell.2015.10.017 [PubMed: 26522593]
77. Dar S, Kamerkar SC, Pucadyil TJ. A high-throughput platform for real-time analysis of membrane fission reactions reveals dynamin function. Nat Cell Biol. 2015; 17: 1588–1596. [PubMed: 26479317]
78. Roux A, Cuvelier D, Nassoy P, Prost J, Bassereau P, Goud B. Role of curvature and phase transition in lipid sorting and fission of membrane tubules. The EMBO journal. 2005; 24: 1537–1545. DOI: 10.1038/sj.emboj.7600631 [PubMed: 15791208]
79. Sorre B, Callan-Jones A, Manneville JB, Nassoy P, Joanny JF, Prost J, Goud B, Bassereau P. Curvature-driven lipid sorting needs proximity to a demixing point and is aided by proteins. Proc Natl Acad Sci USA. 2009; 106: 5622–5626. DOI: 10.1073/pnas.0811243106 [PubMed: 19304798]
80. Aguilo JI, Alonso H, Uranga S, Marinova D, Arbués A, de Martino A, Anel A, Monzon M, Badiola J, Pardo J, et al. ESX-1-induced apoptosis is involved in cell-to-cell spread of Mycobacterium tuberculosis. Cell Microbiol. 2013; 15: 1994–2005. [PubMed: 23848406]
81. Davis JM, Ramakrishnan L. The role of the granuloma in expansion and dissemination of early tuberculous infection. Cell. 2009; 136: 37–49. DOI: 10.1016/j.cell.2008.11.014 [PubMed: 19135887]
82. Schaible UE, Winau F, Sieling PA, Fischer K, Collins HL, Hagens K, Modlin RL, Brinkmann V, Kaufmann SHE. Apoptosis facilitates antigen presentation to T lymphocytes through MHC-I and CD1 in tuberculosis. Nat Med. 2003; 9: 1039–1046. [PubMed: 12872166]
83. Blomgran R, Desvignes L, Briken V, Ernst JD. Mycobač terium tuberculosis inhibits neutrophil apoptosis, leading to delayed activation of naive CD4 T cells. Cell Host Microbe. 2012; 11: 81–90. DOI: 10.1016/j.chom.2011.11.012 [PubMed: 22264515]
84. Aguiló N, Marinova D, Martín C, Pardo J. ESX-1-induced apoptosis during mycobacterial infection: to be or not to be, that is the question. Front Cell Infect Microbiol. 2013; 3: 88. doi: 10.3389/fcimb.2013.00088 [PubMed: 24364000]

85. Choudhary V, Ojha N, Golden A, Prinz WA. A conserved family of proteins facilitates nascent lipid droplet budding from the ER. J Cell Biol. 2015; 211: 261–271. DOI: 10.1083/jcb.201505067 [PubMed: 26504167]

86. Rezwan M, Lanéelle M-A, Sander P, Daffé M. Breaking down the wall: fractionation of mycobacteria. J Microbiol Methods. 2007; 68: 32–39. [PubMed: 16839634]

87. Reis A, Rudnitskaya A, Blackburn GJ, Fauzi Mohd, Pitt AR, Spickett CM. A comparison of five lipid extraction solvent systems for lipidomic studies of human LDL. J Lipid Res. 2013; 54: 1812–1824. DOI: 10.1194/jlr.M034330 [PubMed: 23670529]

Europe PMC Funders Author Manuscripts

Europe PMC Funders Author Manuscripts

Highlights

- Real-time monitoring reveals *Mtb* ESAT-6-mediated phagosome disruption
- Higher surface density of ESAT-6 induces membrane budding and tubulation
- ESAT-6 polymerization drives the rate of vesiculation of the phagosome-like membrane
- ESAT-6 polymerization drives membrane fission by increasing areal strain

Europe PMC Funders Author Manuscripts

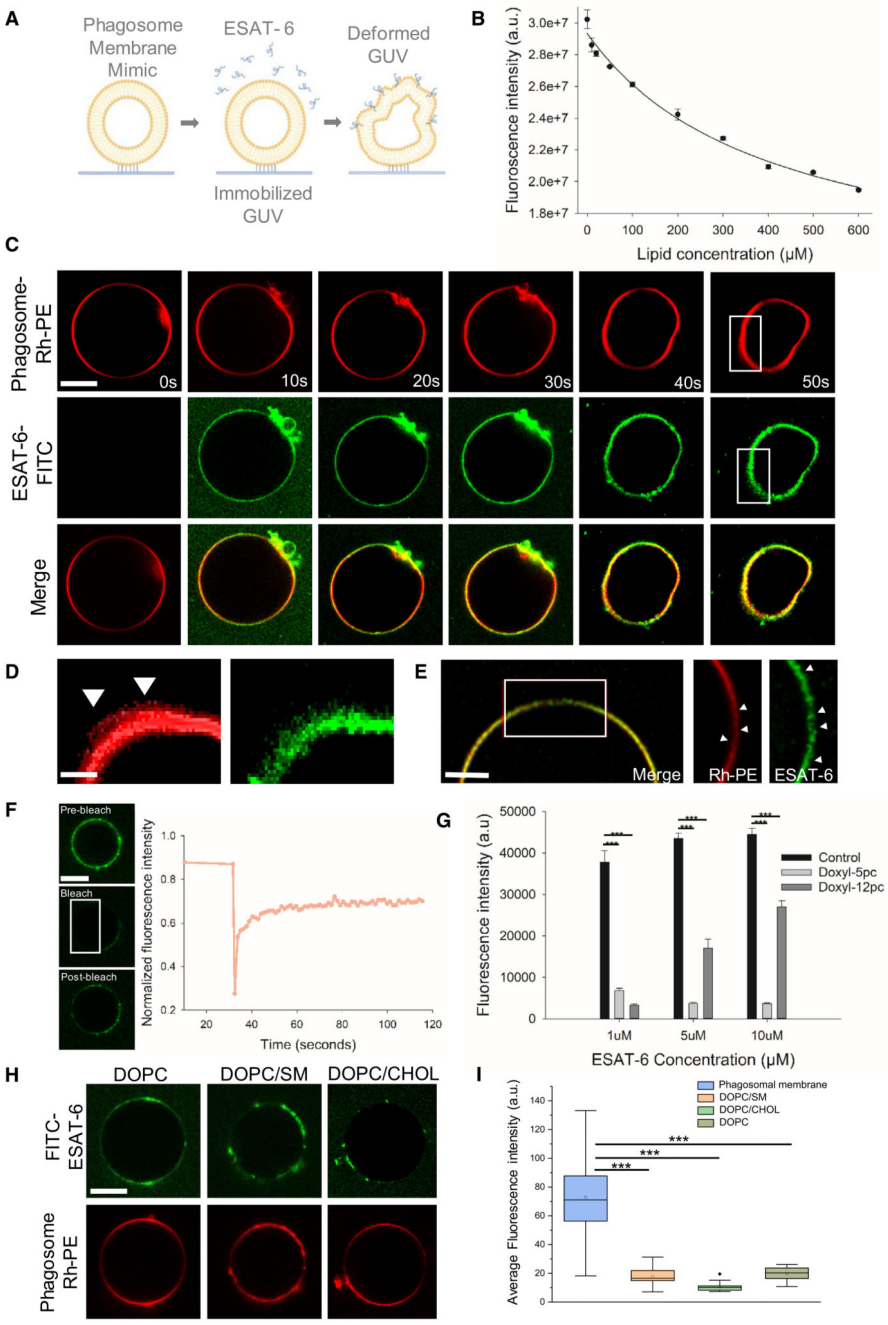

Figure 1. Shallow insertion of ESAT-6 induces changes in phagosomal membrane curvature

(A) Schematic representation of experimental design depicting deformation of the immobilized GUV, mimicking the phagosomal membrane by ESAT-6.

(B) Fluorescence intensity plot of tryptophan residues of ESAT-6 as a function of lipid concentration (LUVs), fitted using hyperbolic decay from a sigma plot. Experiments were carried out in PBS (pH 5.5) at 25°C. ESAT-6 concentration was kept constant at 5 μM. Data points shown are means ± SD of three independent measurements.

(C) Time-lapse confocal imaging of GUVs labeled with 0.1% Rh-PE (red) and incubated with 5 μM FITC-ESAT-6 (green). Scale bar, 5 μm. Images are representative of five independent experiments (n = 73 GUVs).

(D) Zoomed images extracted from (C) represent the curvature change on the membrane. White arrows indicate the ruffle-like structures.

(E) SIM images of GUVs with the same conditions as in (C) followed by zoomed images of the change in membrane curvature. Scale bar, 5 μm (n = 15 GUVs). White arrows indicate the onset of membrane deformation.

(F) Mean fluorescence recovery after photobleaching (FRAP) curves of 5 μM FITC-ESAT-6 on the membrane. Data points using mean values from three independent experiments are shown.

(G) Fluorescence intensity plot of tryptophan residues of ESAT-6 interaction with LUVs (100 nm size) containing 10 mol % of 5-doxyl-PC and 12-doxyl-PC. Data points shown are the means ± SD of nine measurements from three independent experiments. ***p < 0.001 in one-way ANOVA.

(H) Confocal imaging of GUVs of DOPC, DOPC/cholesterol, and DOPC/SM labeled with 0.1% Rh-PE (red) and incubated with 5 μM FITC-ESAT-6 (green). Scale bar, 5 μm. Images are representative of five independent experiments (n = 25 GUVs).

(I) Mean fluorescence intensity plot of ESAT-6 binding for each membrane condition (***p < 0.001 in one-way ANOVA).

Europe PMC Funders Author Manuscripts

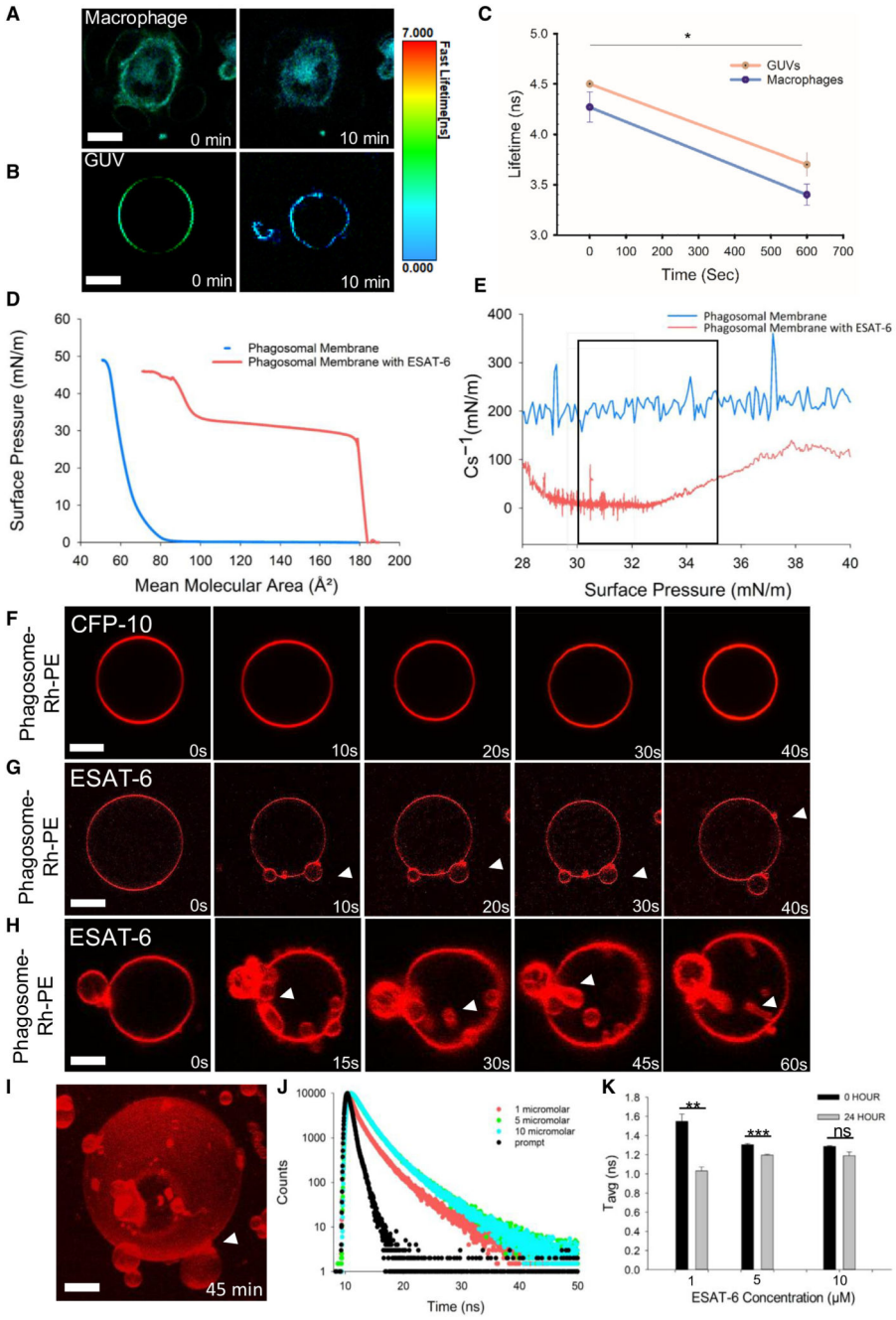

Figure 2. ESAT-6 binding reduces phagosomal membrane tension and compressibility modulus, inducing budding at higher surface density

(A and B) Images from fluorescence lifetime imaging microscopy (FLIM) of FliptR-labeled (A) live macrophages (scale bar, 15 μm) and (B) phagosomal membrane mimic GUV before and after 10 min of 5 μM ESAT-6 treatment (scale bar, 5 μm).

(C) FliptR lifetime measurements of live macrophages and GUVs from three independent experiments as shown in (A) and (B). The data points shown are means ± SD (*$p < 0.05$ in one-way ANOVA).

(D) Surface pressure (π) – mean molecular area (A) isotherm of the phagosomal membrane in the absence (blue) and presence (red) of ESAT-6.
(E) Compressibility moduli (C_s^{-1}) at a surface pressure of 30–35 mN/m (at the bilayer equivalence pressure marked in the rectangular box) are shown in the graph with the same labeling order and color scheme for the membrane conditions as stated in (D). All the monolayer experiments were performed on PBS subphase (pH 5.5) at 25°C. Each isotherm corresponds to the mean of three independent experiments.
(F–H) Time-lapse confocal imaging of immobilized GUVs (same composition and labeling as in Figure 1C) in the presence of higher-concentration (20 μM) (F) CFP-10 and (G and H) ESAT-6. Scale bars, 5 μm (n = 14 GUVs for CFP-10 and n = 18 GUVs for ESAT-6).
(I) Three-dimensional projection of budded vesicles on the membrane extracted from the (G).
(J) Time-resolved fluorescence intensity decay plots of 1 (red), 5 (green), and 10 μM (blue) ESAT-6 in the presence of phagosomal membrane mimic LUVs and measured after 24 h. The fluorescence decay plot of the instrument response function (IRF) is shown in black. All the measurements were carried out in PBS (pH 5.5) at 25°C. These are the representative curves from three independent experiments.
(K) The mean fluorescence lifetime plot extracted from (J) and time-resolved fluorescence intensity decay plots of 1, 5, and 10 μM ESAT-6 extracted from Figure S5, in the presence of phagosomal membrane mimic LUVs and measured after 30 min (0 h), and the data points shown are the means ± SD of three independent measurements (**$p < 0.01$ and ***$p < 0.001$ in one-way ANOVA).

Europe PMC Funders Author Manuscripts

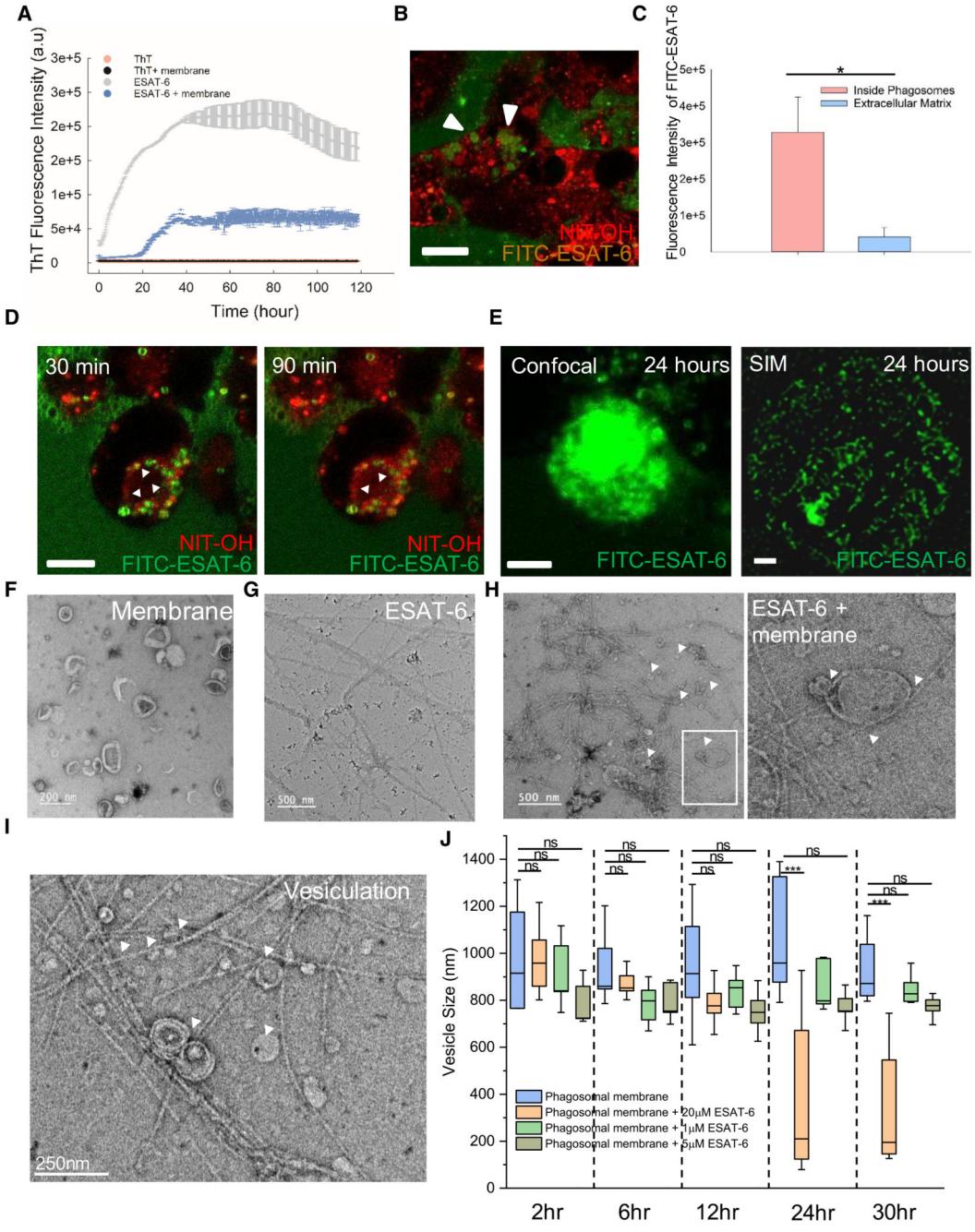

Figure 3. ESAT-6 polymerization facilitates phagosomal membrane vesiculation

(A) ThT fluorescence assay of only 20 μM ESAT-6 (gray) and in the presence of phagosomal membrane mimic LUVs (blue) as a function of time. Data points are shown as the means ± SD of three independent measurements. All the experiments were carried out in PBS (pH 5.5) at 37°C.

(B) THP-1-derived macrophages stained with NIT-OH (red) and treated with FITC-ESAT-6 (green) showing the biogenesis of ESAT-6-encapsulated phagosome-like compartments (highlighted by arrowheads). Scale bar, 15 μm.

(C) Quantification of FITC-ESAT-6 fluorescence intensity through ImageJ of ESAT-6-encapsulated phagosome-like compartments ($n = 150$) and extracellular matrix. *$p < 0.05$ in one-way ANOVA.

(D) Time-lapse imaging of a live cell stained by NIT-OH (red) showing ESAT-6-encapsulated phagosome-like compartments (green). Scale bar, 15 μm. White arrows indicate the ESAT-6-containing phagosomes.

(E) Confocal image and SIM image of THP-1-derived macrophages with 20 μM FITC-ESAT-6 incubated for 24 h. A mesh-like network formed inside cells. Representative images are from a total number of 87 cells observed in different fields of view. Scale bars, 15 μm.

(F–H) Transmission electron micrographs capturing the shape change of the membrane during ESAT-6 fibrillation (F) in only LUVs (scale bar, 200 nm), (G) ESAT-6 fibrils, and (H) budding and vesiculation (white arrows) in the marked inset image at the bottom. Scale bars (G and H), 500 nm.

(I) Mesh-like network of ESAT-6 fibrils around the mother and daughter vesicles. Scale bar, 250 nm. White arrows indicate the budded vesicles attached with the ESAT-6 fibrils.

(J) Vesicle size quantified through dynamic light scattering experiment of only LUVs (blue) and LUVs in the presence of 20 μM (peach), 1 μM (green), and 5 μM (dark green) ESAT-6 monitored for 30 h. The data points shown are the means ± SD of three independent measurements (**$p < 0.01$ and ***$p < 0.001$ in one-way ANOVA).

Europe PMC Funders Author Manuscripts

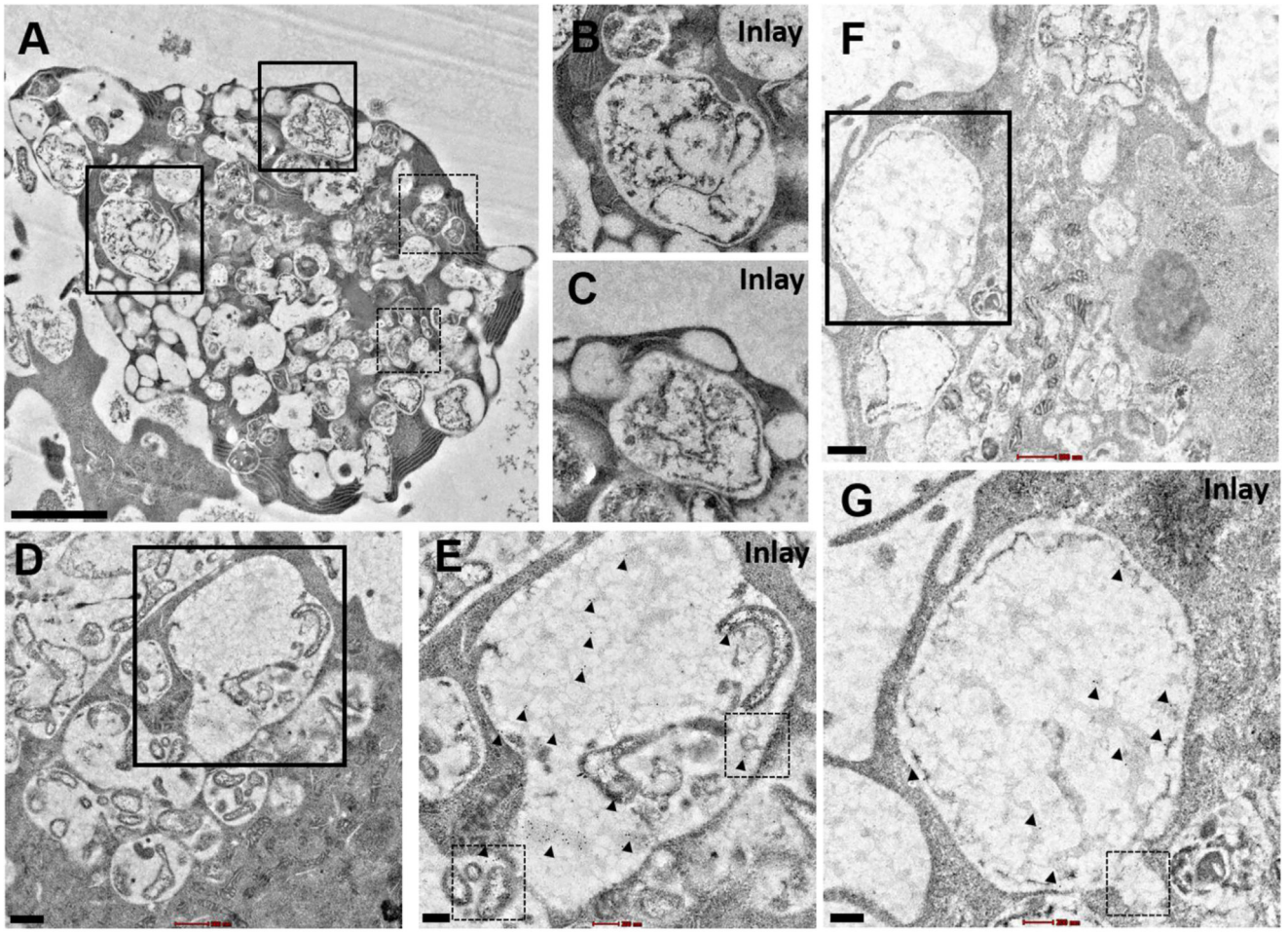

Figure 4. ESAT-6 fibrillation and phagosomal membrane vesiculation inside the macrophage

(A) Representative EM image after thin-section negative staining of macrophages treated with ESAT-6 showing the ESAT-6 fibril-mediated phagosomal vesiculation (highlighted in the dotted black boxes). Scale bar, 1 μm.

(B and C) Inlay images from (A), representing phagosome-like compartments with an ESAT-6 fibril and its subsequent vesiculation of the compartment.

(D) Representative micrograph of phagosome-like compartments containing ESAT-6 labeled with immunogold against hexa-His antibody. Scale bar, 200 nm.

(E) Inlay image from (D) representing ESAT-6 (highlighted by arrows) and vesiculation (highlighted by dotted black boxes). Scale bar, 200 nm.

(F) Representative micrograph of phagosome-like compartments containing ESAT-6 fibrils labeled with immunogold against hexa-His antibody and the compartment vesiculation. Scale bar, 500 nm.

(G) Inlay image from (F) showing the immunogold labeling (highlighted by black arrows) against the hexa-His antibody and the phagosomal vesiculation (highlighted by the dotted black box). Scale bar, 200 nm.

Europe PMC Funders Author Manuscripts

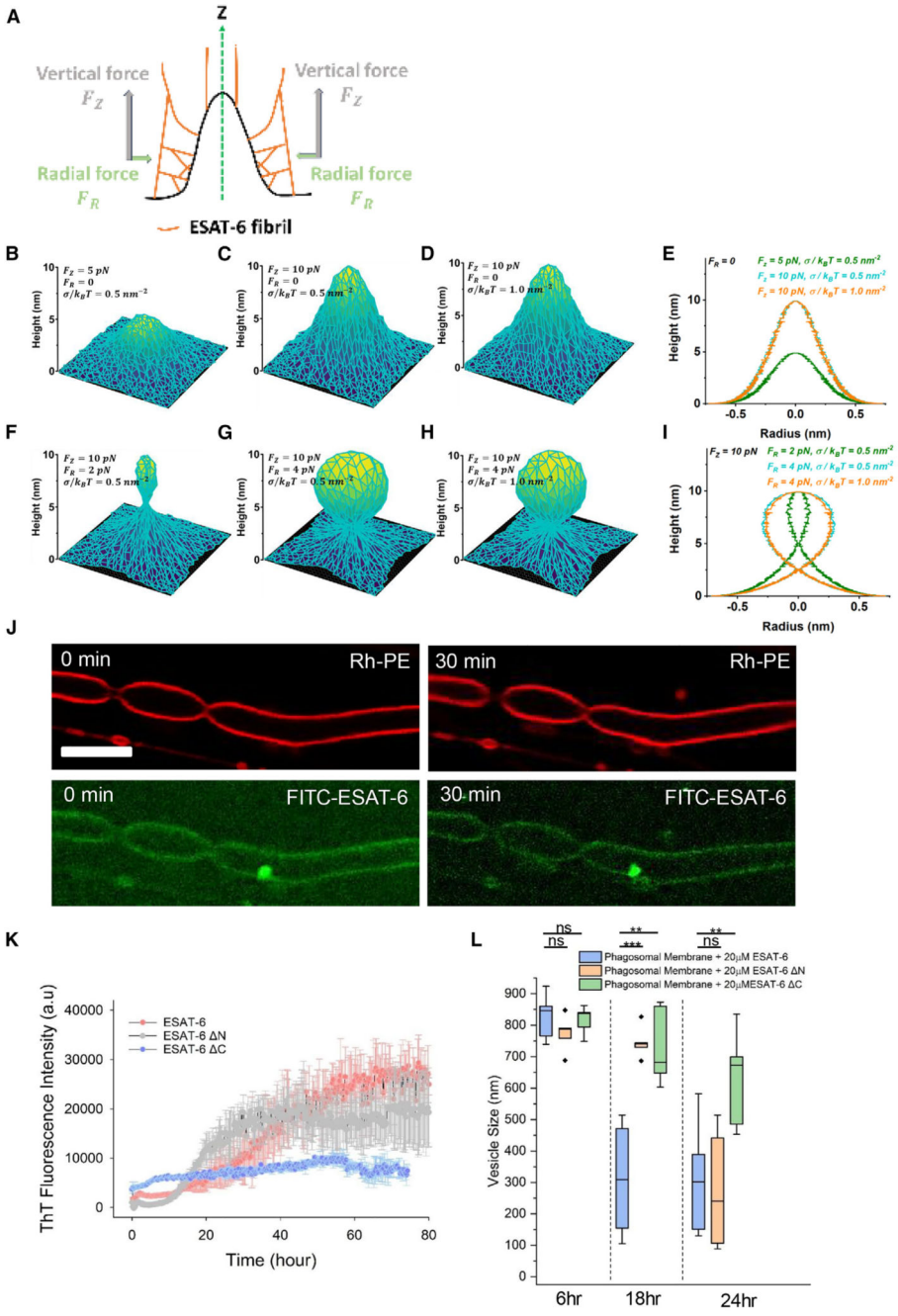

Figure 5. ESAT-6 polymerization forces induce fission

(A) Schematic showing the projections of radial and tangential forces generated by ESAT-6 polymerization.

(B and C) A tubular bud emerges with the application of lateral force, F_Z, while the radial force $F_R = 0$. The surface tension σ is kept at $0.5 k_B T$.

(D) When an elevated surface tension ($\sigma = 1.0 k_B T$) is applied, there are no significant changes in the shape of the tubular bud, even with forces $F_Z = 10\ pN$ and $F_R = 0$.

(E) Two-dimensional representation of the bud growth process depicted in (B) and (C).

(F and G) The radial force introduction results in a more spherical bud shape, with a connecting neck forming between the bud and the membrane. This effect is highlighted under a constant lateral force $F_Z = 10\ pN$.

(F) Even with an elevated surface tension ($\sigma = 1.0 k_B T$), the shape of the spherical bud remains relatively unchanged when subjected to forces $F_Z = 10\ pN$ and $F_R = 4\ pN$.

(I) Two-dimensional representation of radially influenced bud shape shown in (F–H).

(J) Time-lapse confocal imaging of free-floating membrane tubes composed of phagosomal membrane labeled with 0.1% Rh-PE (red) and 5 μM FITC-ESAT-6 (green). Representative images from three independent biological replicates. Scale bar, 15 μm.

(K) ThT fluorescence assay of ESAT-6 and its mutants ΔC and ΔN performed at pH 5.5 and 37°C. Data points are shown as the means ± SD of three independent experiments.

(L) Vesicle size quantified through dynamic light scattering experiment of LUVs in the presence of 20 μM ESAT-6 (blue), 20 μM ESAT-6 ΔN (peach), and 20 μM ESAT-6 ΔC (green) monitored for 24 h. The data points are the means ± SD of three independent measurements (**$p < 0.01$ and ***$p < 0.001$ in one-way ANOVA).

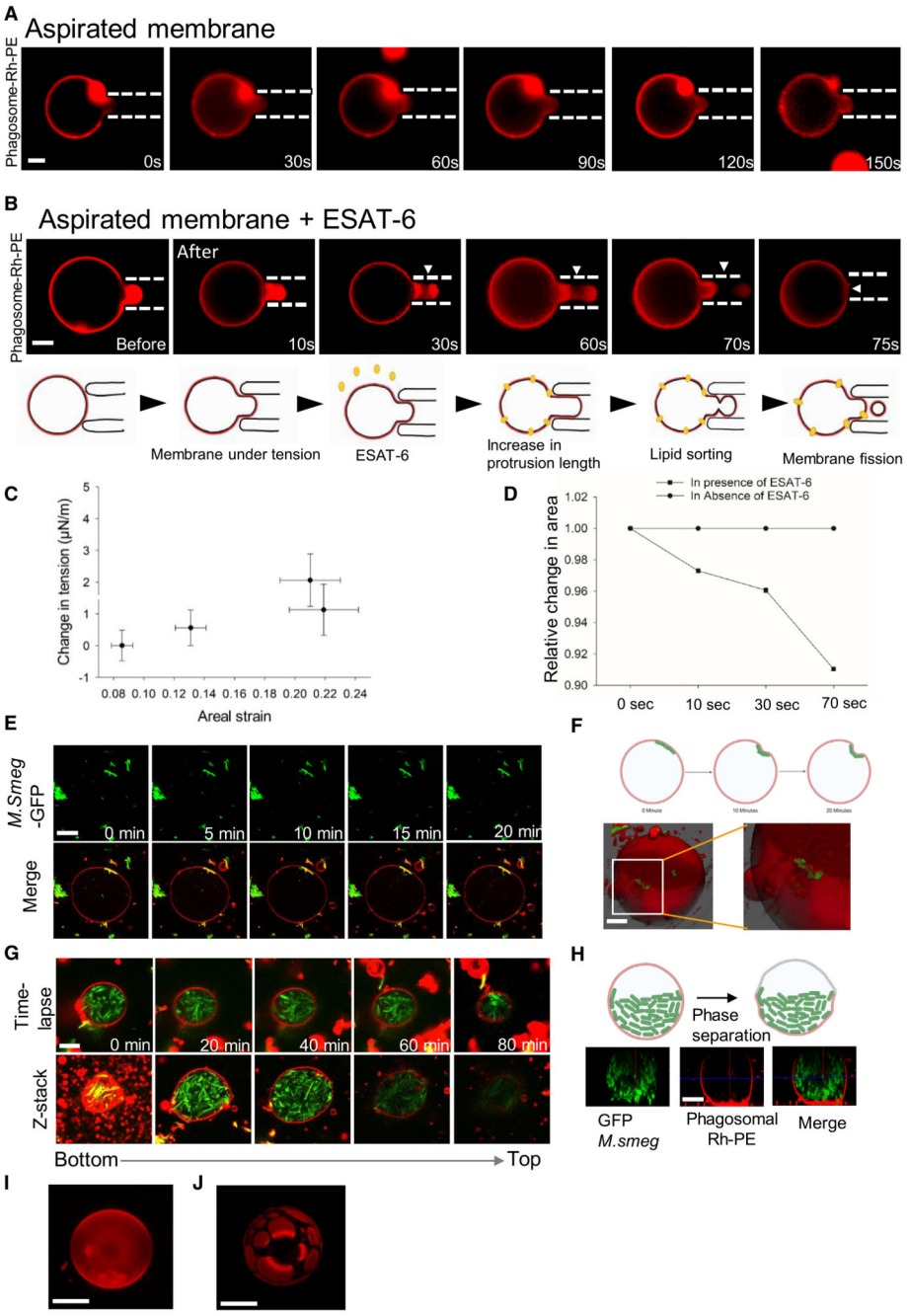

Figure 6. Phagosomal membrane vesiculation proceeds through local modulation of the curvature, lipid segregation, and an increase in areal strain

(A) Time-lapse fluorescence imaging of GUVs labeled with 0.1% Rh-PE (red) aspirated with 50 Pa force and monitored over 150 s.

(B Time-lapse fluorescence imaging of GUVs labeled with 0.1% Rh-PE (red) aspirated with 50 Pa force followed by the addition of unlabeled ESAT-6 and monitored over 75 s. Scale bars (A and B), 5 μm. Images are representative of three independent experiments.

(C) Areal strain versus change in tension plot from (B).

(D) Relative change in membrane area plot from (A) and (B).

Europe PMC Funders Author Manuscripts

(E) Time-lapse confocal imaging of GUVs labeled with 0.1% Rh-PE (red) and immobilized using 0.03% PEG-biotin encapsulated with live *M. smegmatis* (green). Scale bar, 5 μm. Images are representative of three independent experiments.
(F) Schematic and 3D projection of the mycobacteria-mediated curvature change from (E).
(G) Time-lapse confocal imaging and z stack of GUVs labeled with 0.1% Rh-PE (red) encapsulated with the higher load of live *M. smegmatis* (green). Scale bar, 5 μm. Images are representative of three independent experiments.
(H) Schematic and z-stack projection of the mycobacteria-induced membrane phase separation of the membrane from (G).
(I and J) z-stack projections of (I) phagosomal membrane (scale bar, 10 μm) and (J) phase separation induced by the lipid mixing of the phagosomal membrane and the mycobacterial cell envelope at a 1:1 ratio (scale bars, 5 μm) and labeled with 0.1% Rh-PE.

Europe PMC Funders Author Manuscripts

Europe PMC Funders Author Manuscripts

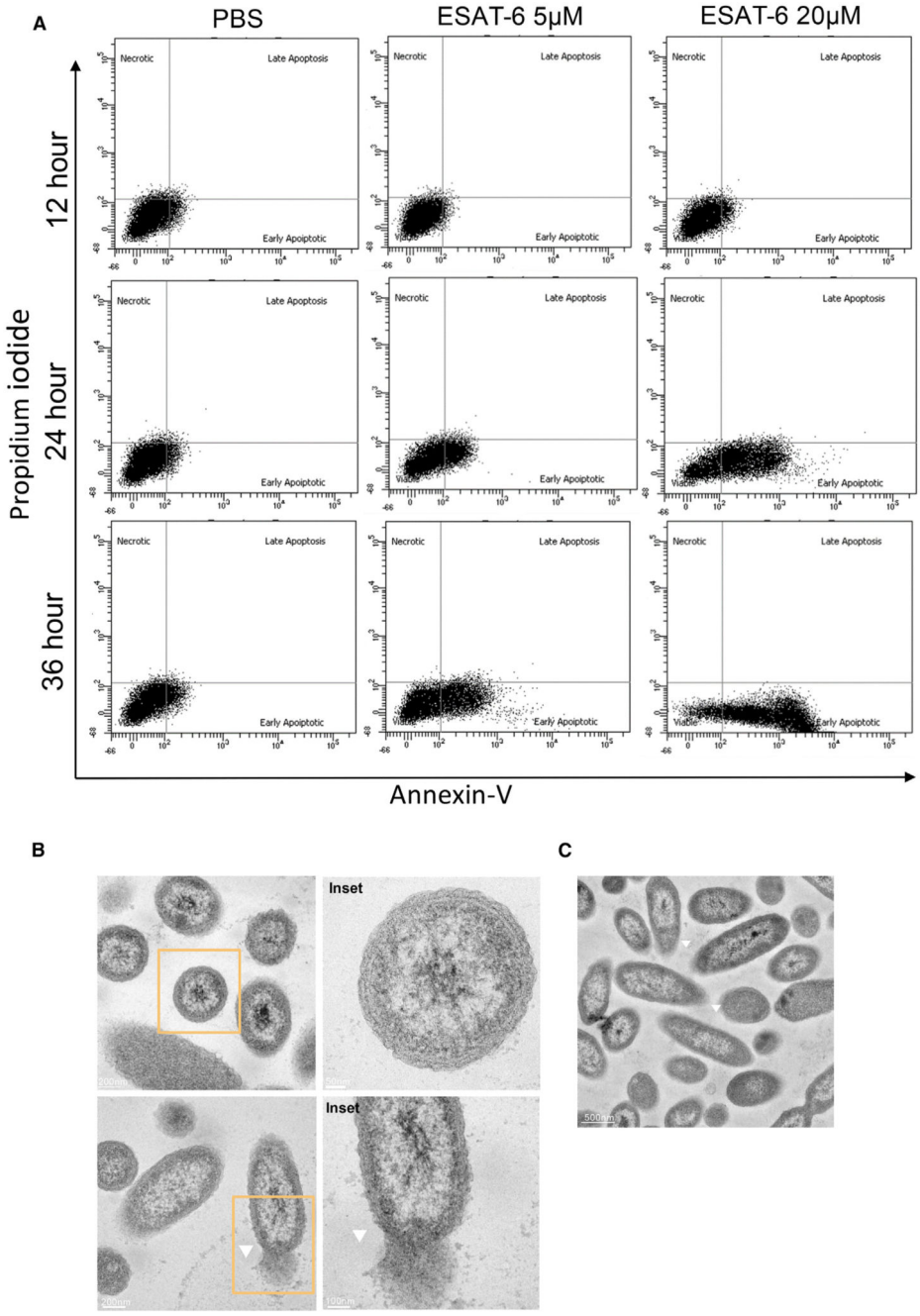

Figure 7. ESAT-6 induced apoptosis and cell death in a concentration- and time-dependent manner

(A) Apoptosis was detected by flow cytometry in macrophage cells after stimulation with ESAT-6 (varying concentrations) at different time points. Lower left (double negative), live cells; lower right (annexin V positive, PI negative), early apoptosis; upper right (double positive), late apoptosis; upper left (annexin V negative, PI positive), necrosis.

(B) Transmission electron micrographs capturing normal cells, with apoptotic cells highlighted in the insets.

(C) Elongated cells with ruptured membranes shown by white arrows. All the cells were treated with 20 μM ESAT-6 followed by incubation for 24 h. These are representative images from three independent experiments.

Europe PMC Funders Author Manuscripts